

# DIAGNOSTIC SYSTEMS ON ALCATOR C-MOD

N. P. BASSE,\*† A. DOMINGUEZ, E. M. EDLUND, C. L. FIORE, R. S. GRANETZ, A. E. HUBBARD, J. W. HUGHES, I. H. HUTCHINSON, J. H. IRBY, B. LaBOMBARD, L. LIN, Y. LIN, B. LIPSCHULTZ, J. E. LIPTAC, E. S. MARMAR, D. A. MOSSESIAN, R. R. PARKER, M. PORKOLAB, J. E. RICE, J. A. SNIPES, V. TANG, J. L. TERRY, S. M. WOLFE, S. J. WUKITCH, and K. ZHUROVICH  
*Massachusetts Institute of Technology, Plasma Science and Fusion Center, Cambridge, Massachusetts 02139*

R. V. BRAVENEC, P. E. PHILLIPS, and W. L. ROWAN  
*Fusion Research Center, University of Texas, Austin, Texas 78712*

G. J. KRAMER, G. SCHILLING, S. D. SCOTT, and S. J. ZWEBEN  
*Princeton Plasma Physics Laboratory, Princeton, New Jersey 08543*

Received September 15, 2005

Accepted for Publication January 14, 2006

*An overview of the diagnostics installed on the Alcator C-Mod tokamak is presented. Approximately 25 diagnostic systems are being operated on C-Mod. The compact design of the machine and the cryostat enclosing the vacuum vessel and magnetic field coils make access challenging. Diagnostics are used to study four focus areas: transport, plasma boundary, waves, and macrostability. There is significant overlap between these topics, and they all contribute toward the burning plasma*

*and advanced tokamak thrusts. Several advanced and novel diagnostics contribute to the investigation of C-Mod plasmas, e.g., electron cyclotron emission, phase-contrast imaging, gas puff imaging, probe measurements, and active magnetohydrodynamic antennas.*

**KEYWORDS:** diagnostics, Alcator C-Mod, tokamak

*NOTE: Some figures in this paper are in color only in the electronic file.*

## I. INTRODUCTION

Alcator C-Mod<sup>1</sup> is a compact (major radius  $R_0 = 0.67$  m, minor radius  $a = 0.21$  m<sup>a</sup>), diverted tokamak with the ability to run high toroidal magnetic field  $B_\phi$  ( $\leq 8$  T), high plasma current  $I_p$  ( $\leq 2$  MA), and high electron density  $n_e$  ( $\leq 1.5 \times 10^{21}$  m<sup>-3</sup>) plasmas. The walls are covered by Mo tiles, and boronization is used regularly to reduce the impurity content of the plasmas. Auxiliary

heating presently consists of ion cyclotron radio frequency (ICRF) minority heating using two 2-strap antennas at 80 MHz and one 4-strap antenna with a variable frequency between 50 and 80 MHz. Additionally, lower hybrid current drive (LHCD) at 4.6 GHz is being brought online, mainly to drive current, but also to heat.

Approximately 25 diagnostic systems are being operated on C-Mod (see Table I). Some diagnostics are mentioned in the table but not described in the paper, such as the neutral pressure gauges shown in Fig. 1. The compact design of the machine and the cryostat enclosing the vacuum vessel and magnetic field coils make access challenging. Ten horizontal ports exist on the outboard side, along with top and bottom ports at the same toroidal positions. Ports are named A through H and J and K; two outboard limiters are installed, a full limiter in the GH sector and a split limiter in the AB sector.

We group the C-Mod diagnostics into four focus areas: Transport (Sec. II), plasma boundary (Sec. III), waves (Sec. IV), and macrostability (Sec. V). There is

\*Current address: ABB Switzerland Ltd., Corporate Research, Segelhofstrasse 1, CH-5405 Baden-Dättwil, Switzerland  
†E-mail: nils.basse@ch.abb.com

<sup>a</sup>Typical values, depend on the magnetic configuration of a given plasma. In this paper, plasma radius mapped to the outboard midplane is labeled using two main types of notation: major radius, identified as either  $R$  or  $R_{mid}$ , and normalized minor radius  $\rho = r/a$ . For standard geometry,  $0.67$  m (axis)  $\leq R \leq 0.88$  m (outboard midplane edge), and by definition  $0.0$  (axis)  $\leq r/a \leq 1.0$  (edge).

TABLE I  
Diagnostic Systems on Alcator C-Mod

Transport
Bolometry Neutron flux Electron cyclotron emission Thomson scattering Two-color interferometer Visible continuum imaging X-ray spectroscopy Charge exchange recombination spectroscopy Motional Stark effect Beam emission spectroscopy Magnetic fluctuation coils Phase-contrast imaging Reflectometry Pellet injection
Plasma Boundary
Video cameras Vacuum UV spectrometry Gas puff imaging Visible spectrometers Soft X-rays Probe measurements Neutral pressure gauges Single-view $H_{\alpha}$ detectors Multi-spatial-point $H_{\alpha}$ arrays
Waves
H/D isotope measurements Compact neutral particle analyzer Hard X-rays
Macrostability
Equilibrium magnetics Active MHD antennas

significant overlap between these topics, and they all contribute toward the burning plasma and advanced tokamak thrusts. Existing diagnostics are continually upgraded and new diagnostics progressively installed to take advantage of new techniques and/or technology and to address new physics questions. We end the paper by discussing recent developments and future diagnostics in Sec. VI.

Measurements are usually digitized using computer automated measurement and control (CAMAC) modules, peripheral component interconnect (PCI) boards, and compact PCI (cPCI) boards. Hardware is controlled by model data system plus<sup>2</sup> (MDSplus) on Linux-based personal computers (PCs).

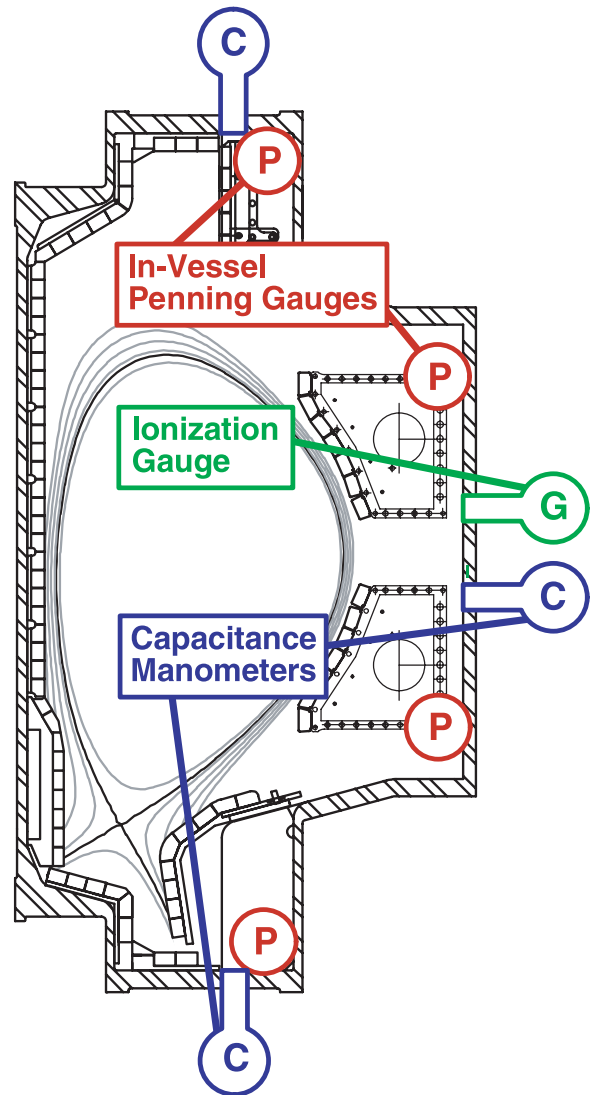


Fig. 1. Three types of gauges are used to monitor gas pressure in the divertor and main chamber regions of C-Mod. These include cold cathode Penning ionization gauges mounted on the wall of the vacuum vessel (P), absolutely calibrated capacitance manometer gauges (C), and Bayard-Alpert-type ionization gauges (G). Gauges C and G are magnetically shielded and located outside the influence of the toroidal magnetic field at the ends of diagnostic ports. The Penning gauges use the intrinsic magnetic field for operation and are an adaptation of a commercially available unit.

## II. TRANSPORT

### II.A. Bolometry

Measurements of the total radiated power using bolometry are performed with two types of detectors. The gold foil bolometers of Ref. 3 provide highly stable and radiation-resistant detectors that can be calibrated

electrically in situ, but with limited signal bandwidth. Semiconductor absolute extreme ultra violet (AXUV) detectors<sup>4</sup> are available in more compact multidetector arrays and have extremely fast response. However, they are known to degrade as a result of radiation damage, and so their calibration is less certain. Cross calibration enables us to take advantage of the strengths of both types of detector.

C-Mod possesses tangentially viewing 16 element arrays of both gold foil and AXUV bolometers, located near the midplane. These provide radial profiles of radiation in the main chamber (confined plasma) by Abel inversion. In addition, poloidally viewing bolometer arrays specifically designed to reconstruct radiation in the divertor have been used to give insights into such phenomena as divertor detachment.<sup>5</sup> A higher spatial resolution tangential edge AXUV array has been used for diagnosis of, for example, the high-confinement mode (H-mode) pedestal.<sup>6</sup>

In addition to the arrays, a detector of each type has been configured to observe the entire plasma. These so-called  $2\pi$  bolometers give a signal proportional to the total radiated power. Their interpretation involves geometric approximations, but the approximations prove to be quite robust and, except in situations of dominant divertor radiation, generally give good agreement with the total main chamber radiation reconstructed by the bolometer arrays. For operational guidance the  $2\pi$  bolometers prove to be extremely useful.

## II.B. Neutron Flux

The total neutron flux is measured using two different systems. The first consists of 12 fission chambers of varying sensitivity combined with four BF<sub>3</sub> counters and four <sup>3</sup>He detectors. These are distributed between four moderator-filled cans at different locations in the C-Mod cell.<sup>7</sup> Two of these are absolutely calibrated with <sup>252</sup>Cf, and the others are cross calibrated from these using the fusion neutrons from C-Mod. The arrangement provides a good dynamic range, but the time resolution is limited to 1 ms because they are operated in count rate mode.

The second detector system is made up of 14 <sup>3</sup>He filled proportional counters surrounded by a polyethylene moderator. Their outputs are connected in parallel, producing a small current proportional to the impinging neutron flux. Measurements of this current can be done with a time resolution of 0.1 ms and are limited only by the slowing-down time of the thermonuclear neutrons in the moderator. Sawtooth oscillations can clearly be seen in the output of this system. The magnitude of the output is scaled to that from the absolutely calibrated system to provide a fast measurement of the total neutron production.

Since the C-Mod plasma is heated solely by ICRF and Ohmic heating, the central ion temperature  $T_i$  can be inferred from the total neutron production. The neutron

production rate is related to the D ion density  $n_i$  and velocity as given by

$$R_{DD} = \frac{n_D^2}{2} \langle \sigma v \rangle_{DD}, \quad (1)$$

where  $\langle \sigma v \rangle_{DD}$  is the value of the D fusion cross section averaged over the velocity distribution function.<sup>8</sup> When  $T_i$  is below 25 keV, the following approximation can be used:

$$\langle \sigma v \rangle_{DD} = 2.33 \times 10^{-14} T_i^{-2/3} e^{-18.76 T_i^{-1/3}}, \quad (2)$$

where  $T_i$  is in keV (Ref. 9).  $n_e$  is corrected from the measured plasma effective charge  $Z_{eff}$  to obtain  $n_i$ , also accounting for the H minority fraction, which is obtained from the ratio of H $_{\alpha}$  to D $_{\alpha}$  line radiation (see Sec. IV.A).  $T_i$  is then found iteratively, assuming that the  $T_i$  profile is Gaussian with the width of the electron temperature ( $T_e$ ) profile.

## II.C. Electron Cyclotron Emission

C-Mod has a set of several instruments measuring the electron cyclotron emission (ECE). This enables routine measurements of  $T_e$  profiles and, taken together, they provide excellent frequency coverage and spatio-temporal resolution. All instruments use second-harmonic extraordinary (X) mode emission, which at the high densities and fields typical of C-Mod provides good optical depth from the center to near the separatrix and is not cut off under most operating conditions of interest. The frequency of this emission is up to 500 GHz at a central  $B_{\phi}$  of 8 T, higher than on most other experiments and affecting our choice of techniques.

A large-scan Michelson interferometer has been operational on C-Mod since its first campaign. This novel instrument, which was designed at the Massachusetts Institute of Technology (MIT), features a large 3-cm stroke, giving a resolution of 5 GHz (Refs. 10 and 11). The mechanical design allows operation up to 33 Hz, with low vibration. The entire instrument is operated under vacuum to avoid H<sub>2</sub>O absorption features in the higher frequency range. Broadband, He-cooled InSb detectors enable measurements of the entire spectrum over about 100 to 750 GHz, typically covering the first three harmonics and allowing  $T_e(r)$  measurements at all  $B_{\phi}$  as well as a check that the emission is thermal.

The viewing optics and transmission beamline for this system consists of a large-aperture Gaussian telescope. Two 20-cm parabolic mirrors, with 2.7-m focal length, image emission from a chord near the horizontal midplane to a variable aperture at the input to the Michelson interferometer.<sup>12</sup> The beamline is also evacuated, with a window separating the instrument and torus vacua. The final mirror is rotatable, allowing the vertical position of the plasma focus to be adjusted or turned to face

an in situ calibration source. This large-aperture, vacuum-compatible source features epoxy tiles cooled by liquid  $N_2$ , which can be switched with a separate source at room temperature.<sup>11</sup> The high throughput of the Michelson interferometer allows it to be absolutely calibrated in situ; calibrations have proved reliable and stable over several years. Other ECE instruments are then cross calibrated using plasma emission.

Higher time resolution measurements are provided by two grating polychromators (GPCs), which share the same viewing optics as the Michelson interferometer. The first, named GPC1, is a nine-channel instrument originally designed by the University of Maryland for use on the Microwave Tokamak Experiment (MTX) tokamak.<sup>13–15</sup> A set of gratings allows full radial coverage for any field of interest. The polychromator design gives a frequency resolution  $\Delta f/f \sim 0.009$ . With broadening due to geometric and fundamental effects, the net radial resolution is typically 1 cm. Bandwidths of up to 900 kHz are possible. At a more typical resolution of 10  $\mu s$ , low noise levels of  $\sim 10$  eV are obtained across the profile. Measurements have been used routinely for a wide range of physics studies in C-Mod, including measurements of sawtooth propagation,<sup>15</sup> deposition of ICRF and mode conversion heating through break-in-slope analysis,<sup>16</sup> detection of core and edge magnetohydrodynamic (MHD) modes<sup>17–19</sup> and measurements of the H-mode threshold and pedestal profiles, enhanced using a  $B_\phi$  sweep technique.<sup>20,21</sup> A second grating polychromator with 19 channels (GPC2) was added in 1998 (Ref. 22). This instrument, developed for use on the Tokamak Fusion Test Reactor<sup>23</sup> (TFTR), has comparable resolution to GPC1 and has enhanced the flexibility of the diagnostic set by increasing the number of measurement channels and enabling two frequency ranges (and two  $B_\phi$ ) to be easily covered in a single experimental day.

A heterodyne ECE system, the Fusion Research Center ECE (FRCECE) diagnostic, was commissioned in 1999. It uses separate viewing optics and enables even higher spatio-temporal resolution measurements.<sup>24</sup> This diagnostic uses in-vessel optics, located for space reasons below the horizontal midplane, to give a narrow Gaussian beam waist and a poloidal resolution of about 1 cm (Refs. 25 and 26). Emission is coupled to a short overmoded waveguide transmission line and detected using a 32-channel radiometer. The frequency range of 234 to 306 GHz was optimized for good radial coverage at  $B_\phi = 5.4$  T, the most common field of operation in C-Mod. This system uses two local oscillators at 115 and 133 GHz and low-noise second-harmonic mixers. Intermediate frequency (if) signals are downshifted to the 4- to 22-GHz band. For profile measurements, a 1-GHz rf bandwidth gives 4-mm radial resolution, with a video bandwidth of up to 1 MHz and very low noise levels. This gives very high resolution measurements of, for example, heat pulse propagation and radio frequency (rf) deposition as well as small quasi-coherent mode fluctu-

ations (Refs. 26 and 27) and fast dynamics at the transition from the low-confinement mode (L-mode) to H-mode.<sup>28</sup> Typical  $T_e$  profiles of several ECE diagnostics, and comparison with Thomson scattering (see Sec. II.D), are shown in Fig. 2.

Correlation ECE (CRECE) measurements aimed at detecting turbulent  $T_e$  fluctuations have also been made with the heterodyne system, using a technique of correlating radially adjacent but disjoint channels to average out thermal noise. A separate if section with three filter pairs of 500-MHz channels was used in addition to the receiver described above. In contrast to results on other experiments,<sup>29</sup> no broadband turbulent fluctuations were detected above the noise level. An upper bound to the fluctuation level was set at about 1% (Ref. 30). The diagnostic is mainly sensitive to fluctuations with  $k_\theta < 5.1$   $cm^{-1}$ . It is possible that fluctuations are lower on the off-midplane view of these optics than on the midplane.

## II.D. Thomson Scattering

A Thomson scattering (TS) diagnostic is used to measure profiles of  $T_e$  and  $n_e$ . The diagnostic has two major components, a core TS and an edge TS system, measuring  $T_e$  and  $n_e$  in these respective regions of the plasma. The core TS system consists of two parts: the original diagnostic that collected first data in 1995 (Refs. 31 and 32) and a 2002 upgrade.<sup>33</sup> High-resolution edge TS (Ref. 34) has complemented the core systems since 1999. All TS diagnostics operate simultaneously, sharing laser setup, collection optics, and a variety of controlling hardware and software tools.

### II.D.1. Diagnostic Setup

The diagnostic uses two identical quality-switched (Q-switched) Nd:YAG lasers ( $\lambda_0 = 1064$  nm) controlled remotely by a PC. Each laser has a fixed pulse rate of 30 Hz, with a nominal 1.3-J, 8-ns pulse. The triggers for

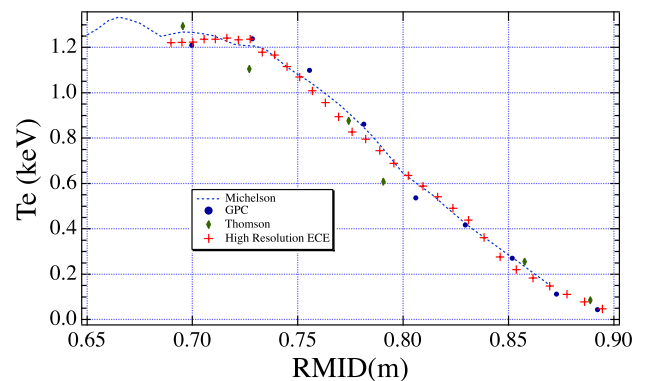


Fig. 2.  $T_e$  profiles from ECE diagnostics (Michelson, GPC, and high-resolution ECE) and Thomson scattering for a typical 5.4-T C-Mod discharge.

flash lamp pumping and Q-switch pulses are generated by CAMAC hardware, set up to provide two staggered Nd:YAG pulse trains and subsequent measurement of TS profiles at 60 Hz. Each Nd:YAG beam is coaligned with a continuous wave (cw) HeNe laser to assist in alignment of the beams through the tokamak vessel. The two beam paths are made close to parallel ( $\Delta\theta \sim 5$  mrad) and directed along a 15-m-long beam path to a vertical port positioned over the tokamak vessel. A pair of remotely controlled steering mirrors on the laser optical bench are used to make fine adjustments to one or both of the beam positions on top of the machine. Each mirror stage tilts in response to two actuators driven by dc motors. Laser beam steering, system temperature control, and real-time system monitoring are accomplished with programmable logic controller (PLC) modules.

From the top of the tokamak, the beams are directed vertically through a focusing doublet with a focal length of 3 m and into the tokamak, entering and exiting through windows placed at the Brewster angle and allowing almost complete transmission of the linearly polarized Nd:YAG beams. The Nd:YAG beams are focused such that the nominal beam width is less than 2 mm along the vertical chord passing through a typical C-Mod plasma. The tokamak poloidal cross section in Fig. 3 shows the beam path through the vessel. Also shown are contours of constant poloidal flux obtained from equilibrium fit<sup>35</sup> (EFIT). The beam paths are nearly collinear throughout the plasma, and scattering from a given vertical location

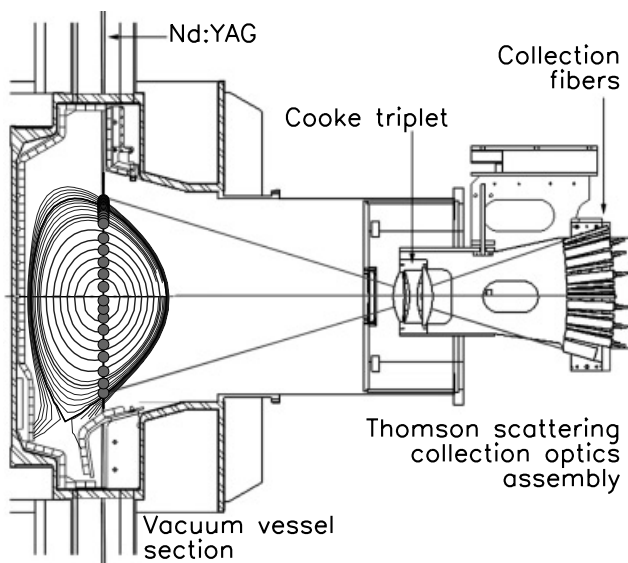


Fig. 3. Cross section of the C-Mod vacuum vessel with contours of constant poloidal flux for a sample plasma discharge. The TS collection optics is mounted such that a Nd:YAG laser beam passing along a vertical chord through the plasma is imaged onto a set of optical fibers. Circles along the beam path represent scattering volumes.

can be assumed to occur at the same radius for either laser.

Shown also in Fig. 3 are the TS collection optics and sample ray traces. Thomson scattered light leaves the vessel through a vacuum window at a horizontal port and is collected at an aperture of  $f/7$  by an air-spaced Cooke triplet. This triplet has a focal length of 30.8 cm and a 1:2 demagnification, with minimal aberration. At the focal surface of the triplet are the TS collection fibers, mounted upon a vertical tilt plate.<sup>33</sup> The fiber positions, together with the radial location of the Nd:YAG beams, determine the vertical location of the scattering volumes. The height of each scattering volume is roughly two times the vertical dimension of its corresponding collection fiber, and it is this dimension that determines the spatial resolution of a given TS channel.

Twenty-two polymer-clad single-strand quartz fibers with a 1-mm active diameter make up the edge TS collection fiber array. These fibers are mounted closely together near the bottom of the focal surface and view the upper edge of C-Mod plasmas, while the remainder of the plasma is viewed by core TS collection fiber bundles. The original core TS system has up to six fiber bundles, which employ glass prisms as light concentrators with an extent of approximately 1 cm along the focal surface. Eight fiber bundles, each 0.4 cm in lateral extent, were added as part of the 2002 TS upgrade. The smaller size allows both improved spatial resolution in a given TS channel and closer spacing between fibers. Figure 3 indicates the locations of scattering volumes for one possible arrangement of collection fibers. A midplane radial resolution  $\Delta R$  of 1 cm can be achieved for certain regions of interest [e.g., internal transport barriers (ITBs)] using core TS, while edge TS gives  $\Delta R \sim 1$  to 2 mm in the vicinity of the last closed flux surface (LCFS).

Collected TS photons are transmitted to an assortment of polychromators designed to detect scattered light falling into distinct spectral bands near the Nd:YAG laser line. The polychromators are each constructed with a relative aperture of  $f/3.5$ , and all use temperature-stabilized Si avalanche photodiodes (APDs) for detection. The response of each APD is digitized with CAMAC hardware. Timing for this pulsed data acquisition is provided by a portion of Nd:YAG light that leaks through steering mirrors as the beam is directed to the tokamak.

The original core TS diagnostic employs Wadsworth mount grating polychromators<sup>31</sup> connected to the set of fiber bundles and light concentrators described above, and the upgrade consists of four channel filter polychromators<sup>36</sup> fabricated by General Atomics, modified to accept an input 0.4-cm fiber bundle at  $f/3.5$ . A single-filter polychromator<sup>37</sup> with multiple spatial channels is employed for the edge TS system, where each channel is reserved for a single 1-mm-diam edge TS fiber. Figures 4a, 4b, and 4c show typical spectral response functions  $f_i(\lambda)$  for these three instruments, where  $i$  is the spectral channel number. The configuration of  $f_i$  in

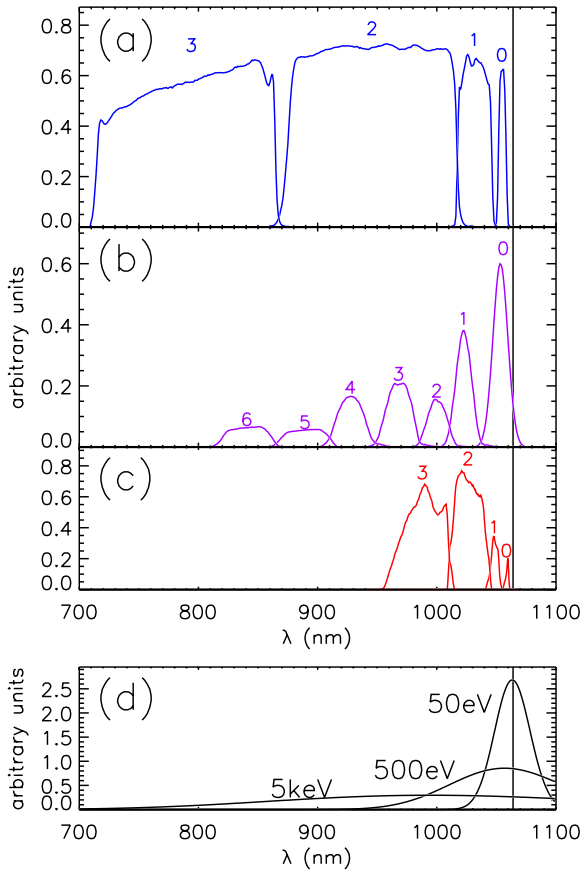


Fig. 4. Typical spectral responses of (a) the core TS upgrade polychromators, (b) the original core spectrometers, and (c) the edge TS polychromator. The vertical line at  $\sim 1064$  nm represents the Nd:YAG laser line. (d) TS spectral distribution for a given  $n_e$  at three values of  $T_e$ .

wavelength space and the width of the TS spectrum as a function of temperature determine the useful  $T_e$  range of each instrument. This range is approximately 0.2 to 5 keV for the original core TS system and  $\sim 0.05$  to 10 keV for the core TS upgrade. The upper bound in  $T_e$  for the edge TS system is reduced relative to the core systems, due to the narrower range in wavelength shown in Fig. 4c. However, the closer distribution of spectral channels near the laser line gives a smaller lower bound and a range of  $15 \leq T_e$  (eV)  $\leq 800$  results, yielding more useful measurements near the LCFS. The dynamic range in density is determined by the signal-to-noise ratio (lower limit) and detector saturation (upper limit). These conditions yield an estimated range of  $0.5 \leq n_e$  ( $10^{20} \text{ m}^{-3}$ )  $\leq 50$  for the original core TS system,  $0.5 \leq n_e$  ( $10^{20} \text{ m}^{-3}$ )  $\leq 30$  for the core TS upgrade, and  $0.3 \leq n_e$  ( $10^{20} \text{ m}^{-3}$ )  $\leq 5$  for the edge TS system.

### II.D.2. Calibrations and Measurements

The shape of the TS spectrum observed from a given scattering location is a known function of  $T_e$  and scatter-

ing angle  $\theta_j$ , where  $j$  is the spatial point number. The amplitude of the spectrum is proportional to both the laser pulse energy  $E_0$  and the local  $n_e$ . Analytical forms of the fully relativistic TS form factor  $S(\lambda, T_e, \theta_j)$  are readily available in the literature.<sup>38,39</sup> Figure 4d shows a sample set of  $S(\lambda)$  at various  $T_e$ . To obtain expected signals from a TS detector as a function of  $T_e$ , we convolve the form factor with the  $f_i(\lambda)$  from Figs. 4a, 4b, and 4c.

Rayleigh and Raman scattering are conventional techniques for the absolute calibrations of TS systems.<sup>40–42</sup> Rayleigh scattering can be used to calibrate the original core TS system only, since the polychromators used in both the upgraded core TS diagnostic and the edge TS system reject the laser line at 1064 nm. All TS systems are spectrally configured to take advantage of Raman scattering in  $\text{H}_2$  and  $\text{D}_2$ , and useful results are obtained for the edge TS system. However, low signals for both core TS diagnostics lead to a high uncertainty in calibration coefficients, undermining the results. For these systems we instead take advantage of cutoffs in ECE that occur due to high plasma densities.

For absolute calibration purposes we make special discharges, during which we ramp the plasma density up to the values critical for the C-Mod ECE diagnostics. During such discharges, the plasma density profile increasingly evolves and as it locally reaches the critical density, an abrupt loss of signal in the ECE channels is observed. Since the ECE diagnostics operate at fixed and known frequencies, the critical density values for all channels where cutoffs are observed can be calculated. Radial positions of the ECE channels are known since the frequency of the emission is proportional to  $B_\phi$ . Thus, we are able to calculate density values at certain positions in the plasma when the ECE channels reach their cutoff. These values are then interpolated in time and space to the measured TS data points and are used to obtain calibration coefficients for the core TS systems. This calibration technique is implemented in situ during regular plasma operation. After several plasma discharges with clear ECE cutoffs for each TS channel, we can determine absolute calibration coefficients for the core TS systems with 10% uncertainty or less.

The edge TS diagnostic takes measurements within  $\sim 2$  cm of the LCFS, a region in which low  $n_e$  results in few cutoffs, and small ECE signals at low  $T_e$  hinder the observation of cutoffs. Moreover, the spatial resolution of the ECE system is very coarse compared to that of the edge TS system, which makes the ECE cutoff calibration method unsuitable for a channel-by-channel calibration of the edge TS diagnostic. This system is calibrated using Raman scattering in  $\text{D}_2$  and  $\text{H}_2$ , and an uncertainty of 15% in the absolute calibration coefficients is obtained. Since C-Mod has some restrictions on filling the machine with a gas other than  $\text{D}_2$ , this form of calibration is typically reserved for the earliest part of a run campaign or is delayed until the end of the campaign.

The TS diagnostic set has been useful to the routine operation of the tokamak, reliably providing accurate and simultaneous measurements of both  $n_e$  and  $T_e$ . In addition, the details of the obtained profiles have been essential to studies of plasma phenomena such as edge transport barriers (ETBs) and ITBs. Figure 5 shows examples of  $T_e$  and  $n_e$  profiles obtained by the TS diagnostics in different plasma regimes. Temperature and density profiles in L-mode are depicted in Figs. 5a and 5b, respectively. Upon transition to H-mode, an ETB forms near the LCFS, creating a region of steep gradients, or a pedestal, in both  $T_e$  and  $n_e$ . The electron temperature in H-mode is shown in Fig. 5c. The  $T_e$  pedestal region is seen to be less than 1 cm in extent, demonstrating the importance of a highly resolved edge TS system. Shown in Fig. 5d is the  $n_e$  profile in a double-barrier regime, where an ITB forms in the presence of the H-mode pedestal. Both barriers are accurately diagnosed by a combination of all three TS diagnostics, and the details of the profiles are used in studies of the formation and evolution of ITBs in C-Mod.

**II.E. Two-Color Interferometer**

The two-color interferometer (TCI) is a vertically viewing 10-chord interferometer using a 20-W, 10.6- $\mu\text{m}$

$\text{CO}_2$  laser, and a 17-mW, 0.632- $\mu\text{m}$  HeNe laser to measure the plasma-induced phase shift and to subtract vibrations.<sup>43</sup> Both laser beams pass through acousto-optic modulators (AOMs), resulting in zeroth- and first-order beams with 40-MHz frequency offsets. The  $\text{CO}_2$  and HeNe beams are then combined to produce coaxial beams that form the plasma and reference arms of the interferometer. Both beams are expanded using reflective cylindrical optics to produce elliptical beams that map properly to the detector arrays (2 mm  $\times$  40 mm). The plasma beam is further expanded to match the required view of the plasma. The C-Mod vertical ports view major radii from 0.6 to 0.8 m. TCI uses only the outer half of this view for all 10 chords since the information on either side of the major axis is generally redundant. The plasma arm passes very close to but does not contact a beamsplitter on its way to the vertical port. After passing through the vessel, the beam is reflected back at a small angle relative to the incident beam for a second pass. The mirror is located on the top of the C-Mod igloo, which provides a very stable, relatively low-vibration-level structure on which to mount this mirror. Vibration levels are typically 100 to 300 HeNe fringes during a C-Mod discharge. On return, the beam strikes the beamsplitter and is combined with the reference beam. Both beams are now properly matched in size to map onto the 10-channel  $\text{CO}_2$  detector array and four

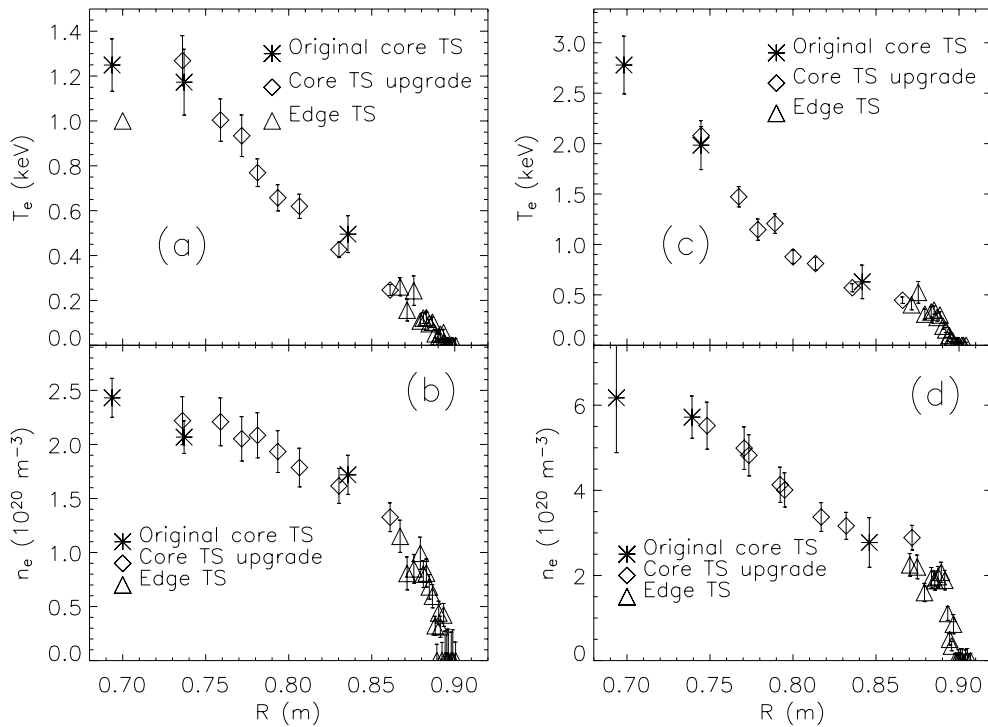


Fig. 5. Typical  $T_e$  and  $n_e$  profiles in different plasma regimes. Only three spatial channels were working in the original core TS system for this plasma discharge. (a)  $T_e$  and (b)  $n_e$  profiles during an L-mode discharge. (c)  $T_e$  profile in H-mode, exhibiting a clear H-mode pedestal. (d)  $n_e$  profile in a double-barrier regime, where an ITB forms in the presence of an H-mode pedestal at the edge. Good agreement between all three C-Mod TS diagnostics is observed for all plasma regimes.

HeNe detectors. All detectors are mounted very rigidly to a common support plate so that once the beams are separated, very little vibration-induced error occurs.

The CO<sub>2</sub> detector array consists of 10 room temperature HgCdTe  $2 \times 2$  mm<sup>2</sup> photovoltaic detectors spaced 4 mm apart. The 40-MHz signals from these detectors drive limiting amplifiers that provide a constant-level signal for the phase demodulators. The HeNe detectors are 0.25-mm-diam avalanche Si photodiodes that also drive limiting amplifiers. A local oscillator derived from the AOM drive signal is used as the reference for phase detection. The phase detector consists of an eight-bit counter to keep track of fringes even at very high fringing rates during pellet injection, and a fraction fringe exclusive-or detector with 10-bit resolution. Signal conditioning, phase detection, memory, and CAMAC interface electronics are built into a single-width CAMAC module. The data acquisition rate is typically 5 or 10 kHz, but the electronics is capable of 1-MHz bursts to measure density fluctuations and fast density changes in response to pellet injections.

## II.F. Visible Continuum Imaging

A tangentially viewing, high-spatial resolution (down to 0.7 mm chordal), visible continuum imaging system is employed on C-Mod to monitor profiles of low-energy free-free bremsstrahlung emission from the plasmas. The light is passed through an interference bandpass filter centered at 536 nm with a full width at half maximum (FWHM) of 3 nm. This spectral region is chosen since it is free of strong line radiation from the working gas and impurity species normally found in the C-Mod plasmas. The emissivity is proportional to  $n_e^2 Z_{eff}$  and is weakly dependent on  $T_e$  (Ref. 44). The detector is a one-dimensional (1-D) charge-coupled device (CCD) array with 2048 pixels. Each pixel is 500  $\mu$ m high by 13  $\mu$ m wide and is capable of lineout rates from 250 Hz to 4.5 kHz. Under most conditions, a 1-kHz rate gives an excellent signal-to-noise ratio. The system utilizes a multi-lens periscope to image the light onto the detector, and the tangential view is accomplished with an optically polished 304 stainless steel flat mirror located inside the vacuum chamber in the shadow of a nearby outboard limiter. A pneumatically actuated linear motion feed-through controls a shutter that protects the mirror and vacuum interface window during discharge cleaning and boronization. Chordal coverage extends from 2 cm inside the magnetic axis to about 1 cm outside the LCFS for typical equilibria. With the assumption of toroidal symmetry, the measured brightness profiles are Abel inverted to yield local emissivity profiles. Using the TS measurements of electron density and temperature profiles, the bremsstrahlung data are used to compute  $Z_{eff}$  profiles. Emissivity profiles, at 2-ms intervals, following the dynamics of an H- to L-mode transition after the ICRF heating was turned off, are shown in Fig. 6. As is typi-

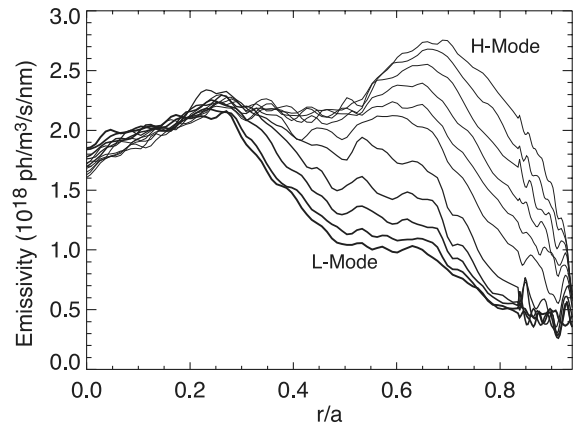


Fig. 6. Visible continuum emissivity profile evolution following an H- to L-mode transition after ICRF heating is turned off in a C-Mod discharge. The profiles, which are plotted at 2-ms intervals, show the evolution that results from the loss of the ETB, leading to a progressive decay of density that propagates inward from the plasma boundary. The traces become bolder as time progresses.

cally the case, after the plasma comes out of H-mode and the edge barrier is lost, the density decrease propagates radially in from the edge; this is reflected in the bremsstrahlung profiles, which are most sensitive to the density evolution.

## II.G. X-Ray Spectroscopy

The current high-resolution X-ray spectrometer system consists of two component parts: three radially viewing, vertically scannable spectrometers and three tangentially viewing spectrometers. The former provide complete radial profiles, out to the LCFS, of parameters such as  $T_i$  and impurity densities, while the latter yield a three-point toroidal rotation velocity profile. Each von Hamos-type spectrometer consists of a variable entrance slit, a quartz crystal ( $2d = 6.687$  Å), and a position-sensitive proportional counter detector.<sup>45</sup> Each spectrometer has a resolving power of 4000, 2-cm spatial resolution, and a wavelength range of 2.7 to 4.1 Å. Spectra are typically collected every 20 ms during a discharge, with 120 mÅ covered at any one wavelength setting. Much of the diagnostic information<sup>46,47</sup> comes from observations of the strongest lines of He- and H-like Ar, introduced by gas puffing.  $T_i$  profiles are determined from the Doppler broadening of the most intense lines; an example is shown in Fig. 7 (Ref. 48).

Toroidal rotation velocity profiles are available by measuring the Doppler shifts; some examples<sup>49</sup> are given in Fig. 8.

Certain line ratios are very sensitive to the electron temperature and can be used to determine the profile

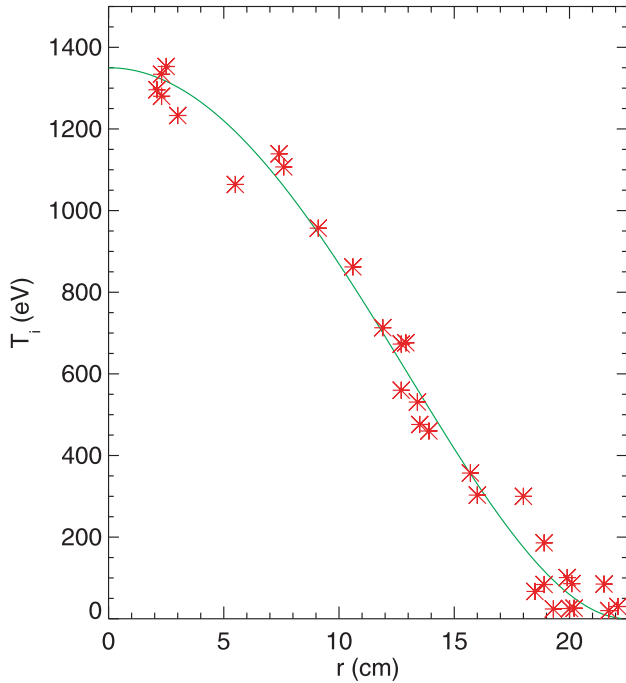


Fig. 7. Ion temperature profile for an L-mode discharge. The asterisks are the measurements and the line is an analytic fit to the data.

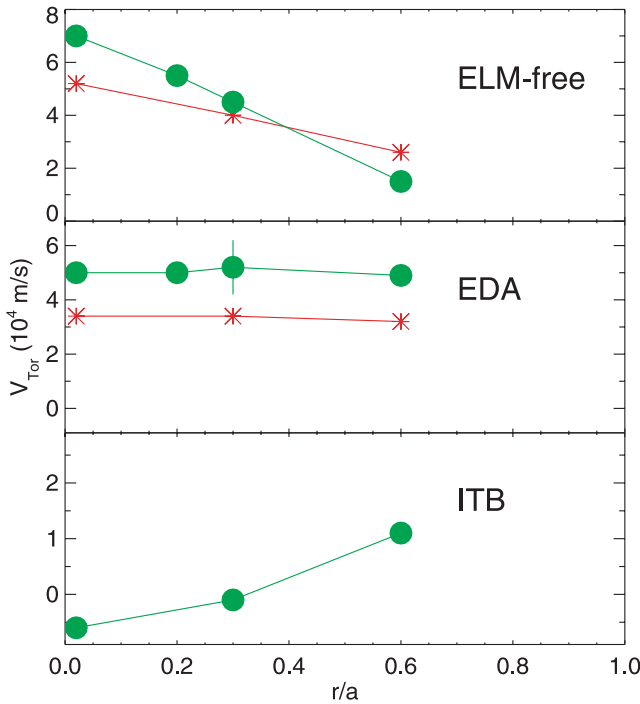


Fig. 8. A comparison of toroidal rotation velocity profiles in two different edge-localized-mode-free H-mode plasmas (top), two different EDA H-mode discharges (middle), and an ITB plasma (bottom).

shape. High- $n$  transitions in Ar, which are populated by charge exchange recombination, have been used to measure the neutral H density profile in the plasma. Absolute line intensities can be used to determine impurity densities, e.g., for intrinsic elements such as Mo (Refs. 50 and 51) and to extract complete impurity density profiles.<sup>48</sup> Intensities of injected impurities can provide information about impurity penetration and screening.<sup>52</sup> Time histories of impurity emission taken along different chords have been used to determine impurity transport coefficient profiles following injection by laser blowoff.  $\Delta n \geq 2$  ground state transitions in charge states of high-Z atoms around Ne-like and medium-Z atoms around He-like have been observed and used to test atomic structure calculations.

## II.H. Beam-Based Diagnostics

### II.H.1. Beam Description

The neutral beam-based diagnostics on C-Mod include charge exchange recombination spectroscopy (CXRS) for  $T_i$ ,  $v_\theta$ , and  $v_\phi$ , beam emission spectroscopy (BES) for density fluctuations, and motional Stark effect (MSE) for  $j_\phi$ . Since C-Mod is not heated with neutral beams, a diagnostic neutral beam (DNB) is used to excite the spectra required for the measurements. The beam used for the 2004 campaign<sup>53</sup> generated a 45-kV H beam. The accelerated current before neutralization was typically 4 A. The neutralized current is computed to approximately 3 A based on measurements of the component mix downstream from the neutralizer and estimates of the neutralizer efficiency for each component. The power supply technology limited the pulse length to 0.1 s. The variation of the beam profile width with accelerating current is shown in Fig. 9. The width of the beam density profile measured at the  $1/e$  points near the beam focus is 8 cm. For later reference, this corresponds to a FWHM between 6.5 and 7.5 cm. Using a cold cathode source,<sup>54</sup> the beam produced the usual four energy components of H neutrals at energies equal to the full beam energy and to one-half, one-third, and one-eighteenth of the beam energy. The densities of these components at the output of the beam (following the neutralizer) were in the ratios 45:8:29:18 as measured spectroscopically during actual experiments.<sup>55</sup> The penetration of the beam into a C-Mod enhanced  $D_\alpha$  (EDA) H-mode plasma is shown in Fig. 10. From this, it is clear that the beam can probe the plasma in the range  $0.75 \text{ m} < R < 0.90 \text{ m}$  or, equivalently,  $0.3 < \rho < 1.0$ . For the 2006 campaign onward, that beam was replaced with one better tailored to C-Mod requirements. With a maximum beam voltage of 50 kV and an accelerated ion current of 7 A, better penetration of the beam into high-density plasmas is achieved. The beam pulse length is 1.5 s continuous or 3.0 s modulated to better match the C-Mod pulse length.

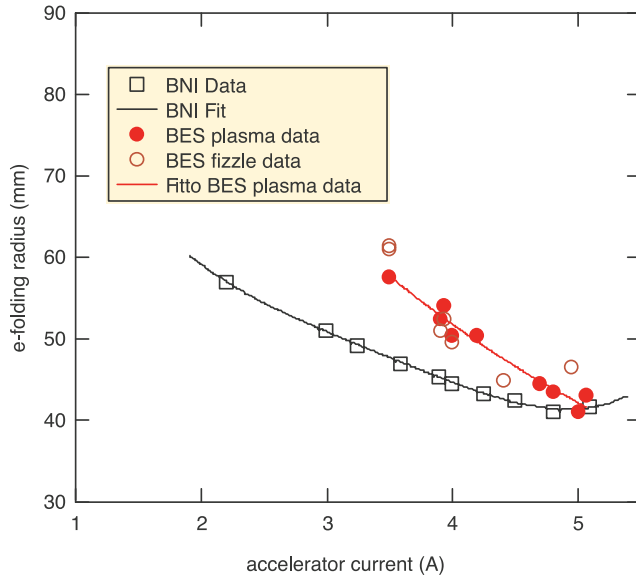


Fig. 9. DNB e-folding radii versus beam current from specifications (black squares and line) and measured by BES (circles and line [red online]). The black points were measured using calorimetry while BES measured emission from only the full-energy beam component.

II.H.2. CXRS

The CXRS optical systems are simple and have high throughput.<sup>56</sup> There are three optical systems in use at

present. These must be designed for in-vessel installation close to the plasma, where they are subject to large forces during disruptions and are inaccessible between vacuum vents. Two toroidal optical systems (see Fig. 11), located in-vessel, provide 10 channels of  $T_i$  and  $v_\phi$  data from  $78.4 \text{ cm} < R < 87.7 \text{ cm}$  with a resolution of 0.5 cm and 10 channels of data from  $76.5 \text{ cm} < R < 87.3 \text{ cm}$  with a resolution of 0.6 cm viewing away from the beam. The latter allow background subtraction in those plasma discharges with a weak CXRS signal strength. A third poloidal system located in-vessel provides 25 channels of  $T_i$  and  $v_\theta$  data from  $84.7 \text{ cm} < R < 90.3 \text{ cm}$ .

The toroidal optical system is protected by shutters that are typically closed during wall conditioning to prevent accelerated degradation of the optics. The first two elements in the toroidal optics are a pair of stainless steel mirrors that direct light from the beam into a lens train. The first lens element is a pair of plano-convex lenses with relative orientation to reduce spherical aberration and coma. To reduce the overall length of the system while limiting aberrations, a meniscus lens was added. The total magnification of the system is 0.2. The beam is imaged onto an image dissector consisting of a set of 10 fiber bundles that transmit the light to the vacuum feed-through. This section of the optical fiber is exposed to the plasma, discharge cleaning, and extremes of temperature due to active heating of the vacuum vessel. Each channel is a  $1 \text{ mm} \times 2.5 \text{ mm}$  bundle of fibers. Each fiber has a  $200\text{-}\mu\text{m}$  fused silica core, a  $10\text{-}\mu\text{m}$ -thick F-doped silica cladding and a  $12.5\text{-}\mu\text{m}$ -thick polyimide jacket. The 10 channels are independently shielded in stainless steel

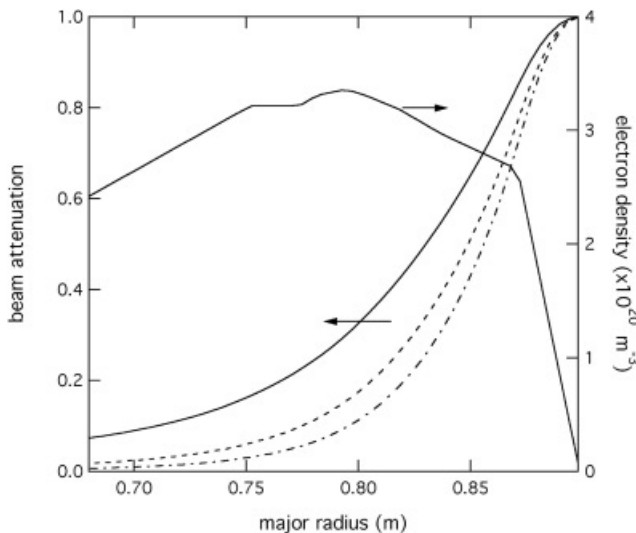


Fig. 10. Simulation of the beam penetration into an EDA H-mode discharge (1031209028 at 1 s). The attenuation of the beam components at the beam energy (solid line), one-half the beam energy (dashed line), and one-third of the beam energy (dotted-dashed line) are shown. A density profile is also displayed.

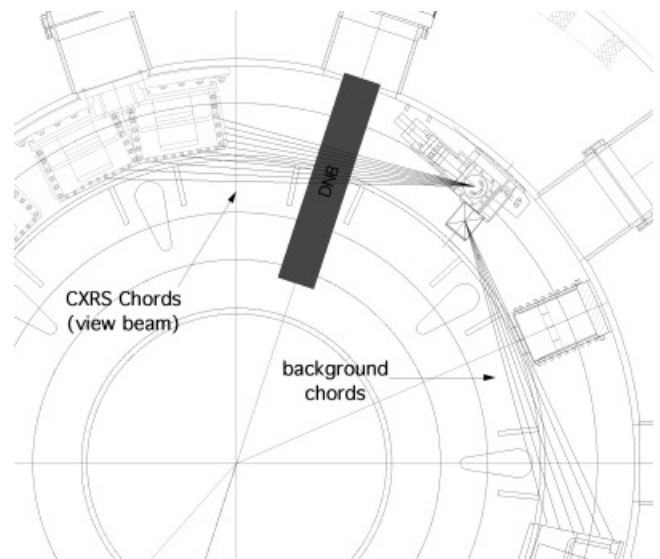


Fig. 11. Location of the toroidal CXRS views during the 2004 and 2005 campaigns. One views the beam and the other views plasma without the beam to use for background subtraction in the event of low CXRS signal levels.

monocoil to improve flexibility and are only assembled into a single unit at the lens end. The vacuum feed-through in each case is a 50-mm-diameter fiber optic faceplate with a 6- $\mu\text{m}$  fiber size. The light is then transmitted through relay fibers to the spectrometer.

The poloidal optics in use at present emphasize measurements in the pedestal region of the plasma. A single achromatic lens focuses the plasma onto a collection of twenty-five 400- $\mu\text{m}$  fibers. The resolution of the system is approximately 3 mm. Rather than a shutter, this system employs an extended tube to prevent the plasma from contacting the lens.

The use of a high-throughput ( $f/1.8$ ) imaging spectrometer (Kaiser Optical Systems, Ann Arbor, Michigan) and a large two-dimensional (2-D) camera as a detector (Roper Scientific Instruments, Trenton, New Jersey) are critical to this experiment. The high density of the plasma and consequent high attenuation of the beam in the outer portion of the plasma reduces the available light in the core, so high throughput is important. The spectrometer forms a 2-D image in its exit plane; this allows as many as 45 fibers, each representing a spectrum from a different spatial view, to be observed simultaneously.

A typical spectrum that is used for CXRS is shown in Fig. 12. The spectrum contains two well-resolved B lines. B is used for the measurements since it is the light impurity with highest concentration. The line used to detect CXRS emission is 4944.67 Å ( $n = 7 \rightarrow 6$ )  $\text{B}^{+4}$ . The line is blended with a line from a lower ionization stage, 4940.376 Å,  $2s3d^1D_2 - 2s4f^1F_3B^{+1}$  (Ref. 57). Shown in blue in Fig. 12 is the spectrum taken just after the DNB was turned off. The spectrum in red during the DNB pulse—in comparison with the spectrum taken after the

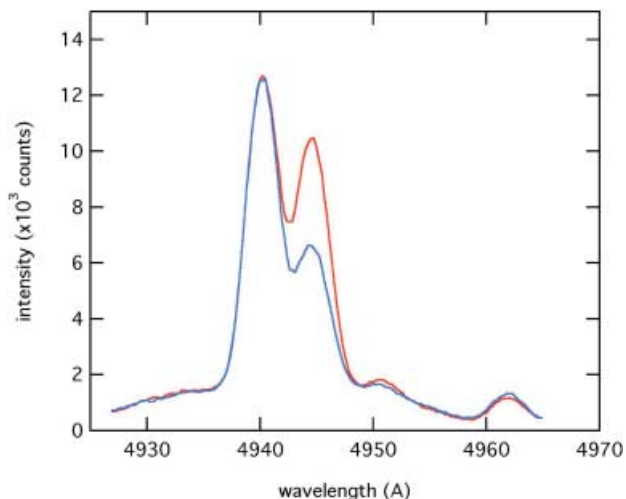


Fig. 12. The line used to detect CXRS emission is 4944.67 Å ( $n = 7 \rightarrow 6$ )  $\text{B}^{+4}$ . It is blended with a line from a lower ionization stage, 4940.376 Å,  $2s3d^1D_2 - 2s4f^1F_3B^{+1}$ . One spectrum (red) is taken during a beam pulse. The other (blue) is taken just after the beam pulse.

DNB was turned off—shows the CXRS enhancement relative to the background  $\text{B}^{+4}$  emission that is excited by electron excitation and thermal charge exchange. The line blend is superposed on the continuum. A detailed model for the line is used to extract  $n_{\text{BII}}$ ,  $n_{\text{BV}}$ ,  $T_i$ ,  $v_\phi$ , and  $v_\theta$ . The model includes a fine structure of the  $\text{B}^{+4}$  line, including a very detailed description of the Zeeman effect, since  $B_\phi$  is typically 5.4 T.

### II.H.3. MSE

Both the MSE diagnostic and BES, described later, observe Balmer- $\alpha$  emission from the beam ( $\text{H}_\alpha$ ). In addition, they share the same optical system at the machine, designed and built primarily by Princeton Plasma Physics Laboratory for MSE with input from the University of Texas Fusion Research Center for compatibility with BES. The lack of convenient tangential access on C-Mod prompted an unusual optical design involving five lenses and three dielectric mirrors tuned to  $\text{H}_\alpha$  inside the vacuum chamber. The in-vessel optical system shown in Fig. 13 views the radially directed DNB across the region  $67 \text{ cm} < R < 90 \text{ cm}$  at a 5 deg downward angle. This is an attempt to view along the magnetic field lines to maximize poloidal resolution for BES. A view vector also has a component parallel with the DNB axis that introduces a Doppler shift that separates the beam  $\text{H}_\alpha$  emission from

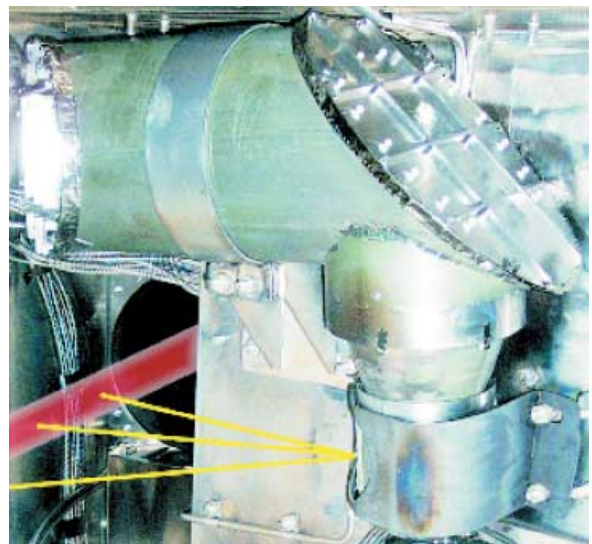


Fig. 13. The MSE/BES in-vessel optical periscope. An artist's conception of the DNB (smaller than actual) and example view chords are indicated in red and yellow, respectively. The light is reflected upward by a mirror behind the entry lens through two additional lenses to another mirror (attached to the ribbed oval plate at the upper right-hand side of the photo). This mirror reflects the light toward the left to a third mirror (the bright plate at the upper left-hand side of the photo), which relays the light out of the vessel.

the edge  $D_\alpha$  emission. However, the angle degrades radial resolution because of the finite beam width (8-cm FWHM). The lenses and mirrors are housed in a periscope assembly (light green in Fig. 13) that relays collected light out of the vessel through a 10-cm-diam window on the same port but 23 cm above the DNB. The light is carried farther out radially by five relay lenses outside the vacuum to an image dissector populated by both MSE and BES collection fibers. The external optics also contain two photoelastic modulators (PEMs) at 20 and 22 kHz oriented at a relative angle of 45 deg and a linear polarizer, all required for MSE. The collection area at the beam is the area of the fiber tips magnified by the optical system. The magnification decreases with major radius from 6.0 at  $R = 67$  cm to 3.8 at  $R = 80$  cm (optical axis) to 3.3 at  $R = 90$  cm.

The use of in-vessel optical components posed several challenges for the optical and mechanical design of the system, since the in-vessel environment is demanding with regard to mechanical forces, magnetic field strength, window coating, temperature (C-Mod is baked to 150°C), and outgassing limitations. Because disruptions induce transient forces on vacuum components, the in-vessel glass components are protected by trapped volumes of Teflon cushioning less than 1 mm thick, and support plates for the larger mirrors are fabricated from INCONEL® to reduce eddy currents. To minimize Faraday rotation, all transmissive optical elements are fabricated from low Verdet SFL6 glass with the exception of the PEMs. A shutter mechanism surrounds the plasma-facing lens that can be positioned in one of three orientations, providing either a direct line of sight to the plasma, or a completely obstructed view (to protect against coating by boronization and large disruptions) or a view through a wire-grid polarizer for MSE calibration purposes.

The MSE diagnostic<sup>58–60</sup> measures the profile of magnetic pitch angle at 10 spatial locations. The radial resolution is limited to  $<1.4$  cm at the plasma edge and  $<5.0$  cm at the plasma center by the finite width of the DNB. Its basic principle of operation is similar to the MSE diagnostic originally implemented on the Princeton Beta Experiment-Modification<sup>61</sup> (PBX-M) with some modifications to accommodate the C-Mod environment. Beam neutrals experience a Lorentz electric field ( $\mathbf{E} = \mathbf{v} \times \mathbf{B}$ ) arising from their motion across the magnetic field, which splits the degenerate Balmer- $\alpha$  emission into a partially degenerate multiplet whose components are polarized relative to the local electric field. It is the polarization direction of the full-energy  $+\pi$  component that is measured.

The image dissector is populated by an array of 1-mm optical fibers that resolve 16 radial locations, of which 10 are used for MSE. The light is carried 35 m to a set of temperature-controlled dielectric filters, each tuned to the full-energy  $+\pi$  Stark component. The photon signals are then converted to current by Hamamatsu R943 photo-multipliers, amplified, and digitized at 1 MHz by D-TACQ ACQ216 cPCI digitizers. The polarization direction of

the  $\pi$ -shifted Stark lines is related to the ratio of the signal amplitude at the second harmonic of the two PEM frequencies. In place of the customary lock-in amplifiers to measure the signal amplitudes at specific frequencies, we employ digital lock-in analysis that determines the amplitude at a given frequency by multiplying the raw digitized signal by a reference sine wave with the desired frequency and with a phase provided by the PEM drive signal. This procedure allows the fast Fourier transform amplitudes to be measured at a variety of harmonics and beat frequencies of the PEMs, which provides useful information about circular polarization of the light as well as the maximum retardation imposed by the PEMs.

Two standard techniques are employed to provide an absolute calibration of the MSE diagnostic. The first involves firing the DNB into the torus filled with low-pressure D gas (0.5 to 2 mTorr). A magnetic field with known pitch angle is generated by the toroidal and equilibrium field coils and serves as a reference for the angles measured by MSE. The second technique mounts a linear polarizer onto a precision rotatable stage positioned in-vessel along the trajectory of the DNB to provide reference linearly polarized light through a full 360 deg.

#### II.H.4. BES

BES (Ref. 62) observes  $H_\alpha$  emission from the DNB without regard to Stark or beam energy components. All light passing through a bandpass filter is collected. Fluctuations in the emission can be translated into plasma density fluctuations. Also, since the system is absolutely calibrated, it can provide, with some modeling of the detected spectrum, radial and vertical profiles of the beam density.

The image plane of the optical system is sampled by thirty-six 1-mm optical fibers in a close-packed  $6 \times 6$  array outside the farthest-out MSE fiber bundle. This arrangement is to allow maximum flexibility in measuring fine-scaled fluctuations in the edge. The array can be moved radially to sample the region  $90 \text{ cm} > R > 87 \text{ cm}$  (86 cm if the edge MSE fiber is removed). The array is restricted to the edge because the angles between the interior views and the beam axis result in averaging over a large radial region. This is a consequence of the purely radial injection of the beam. The angles between the edge views and the beam, in contrast, are close to perpendicular. In addition, there are seven discrete fiber bundles, of two or four 1-mm optical fibers each, which can view a wide range of locations in the plasma above or below the array or the MSE views. These can be used to measure steady-state emission, e.g., beam profile, or large-scale fluctuations in the core.

The fibers carry the light 32 m to an eight-channel filter spectrometer, fashioned after that used on the DIII-D tokamak.<sup>63</sup> From one to four adjacent fibers of the edge array or a single fiber bundle can be input into any channel of the spectrometer. The cone of light emerging from the

fibers of each channel is collected and collimated by a lens and then passes through a six-cavity filter with passband  $6600 \pm 10 \text{ \AA}$  (at normal incidence). The passband is adjusted (lowered) by tilting the filter via a precision micrometer/lever system to pass most of the Doppler-shifted  $H_\alpha$  emission from the beam while mostly rejecting the strong ambient  $D_\alpha$  emission from the plasma edge. The filtered light is then focused by an aspheric condensing lens onto the detector. The magnification of the spectrometer optics (0.4) is chosen to image as many as four fiber tips onto the active surface of the detector. The detectors and electronics are identical to those used on DIII-D (Ref. 63).

With the aid of a spectral model of the beam emission and the bandpass filters, the beam density may be inferred from the raw data. Figure 9 showed measurements of the beam profile measured by the BES system. Radial profiles may also be measured, and since the system is absolutely calibrated, beam performance can be diagnosed.

An example of a density fluctuation measurement is shown in Fig. 14, which shows the coherences and phases (modulo  $2\pi$ ) of three spatial locations (channels 3 through 6) relative to a fourth (channel 2), all located at  $R \sim 88.5 \text{ cm}$ . The feature in the spectrum at 100 to 120 kHz is the quasi-coherent mode seen near the separatrix of EDA H-mode plasmas. Channels 3 through 6 are separated vertically from channel 2 by 0.0,  $-4.5$ ,  $-1.5$ , and  $+3.0 \text{ cm}$ , respectively. The phases are consistent with a downward propagation (electron diamagnetic direction) of 3.5 to 4.0 km/s.

### II.1. Magnetic Fluctuation Coils

The fast magnetic fluctuation diagnostics on C-Mod consist of 65 poloidal field pickup coils mounted on two

outboard limiters in addition to the 26 standard magnetic pickup coils located in four equally spaced toroidal locations.<sup>64</sup> Of the standard set of poloidal field pickup coils, only the four coils nearest the midplane on the inner wall are used for fluctuation measurements, because the others are too far from the plasma to make reliable measurements of small-amplitude fluctuations. There are 29 coils mounted to the sides of the full limiter between the G and H ports and an equivalent set of 24 coils mounted to the sides of the split limiter between the A and B ports. There are also three coils mounted beneath the Mo tiles on both outboard limiters, separated toroidally by about 3.8 cm and located 10 cm above and below the midplane. Figure 15 shows a cross section of C-Mod with the pickup coils mounted to one side of the full limiter as well as the standard coils mounted poloidally around the vessel wall.

The standard magnetic pickup coils are described in Sec. V.A. The coils mounted to the limiter are based on the same design but are only 13 mm long and 8 mm in diameter with four layers of 29 American wire gauge (AWG) (0.287-mm-diam) Kapton coated magnet wire with a total surface area of 47 cm<sup>2</sup>. Kapton was chosen because it is vacuum compatible up to at least 150°C and can insulate well with very thin coatings to allow a larger number of turns in a small-diameter coil. The bobbins are made of 99.8% pure Al<sub>2</sub>O<sub>3</sub> sintered alumina ceramic. To ensure the exact location of the coils for accurate poloidal and toroidal phase measurements even for short-wavelength modes, the coils are mounted with stainless steel blocks aligned with precisely machined holes in the limiter plates at each end of the coil.

The magnetic fluctuation coils were originally digitized with 30 CAMAC channels having 12-bit resolution sampling at 1 MHz for just over 0.5 s and with 18 channels sampling at 2 MHz for just over 0.25 s.

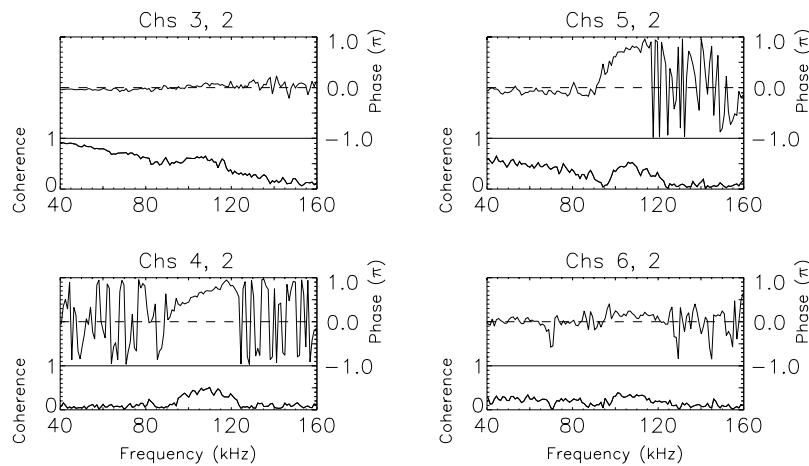


Fig. 14. Coherence and phase between various BES views at  $R = 88.5 \text{ cm}$ . Channels 3, 4, 5, and 6 are separated vertically from channel 2 by 0.0,  $-4.5$ ,  $-1.5$ , and  $+3.0 \text{ cm}$ , respectively. The feature at 100 to 120 kHz is the quasi-coherent mode.

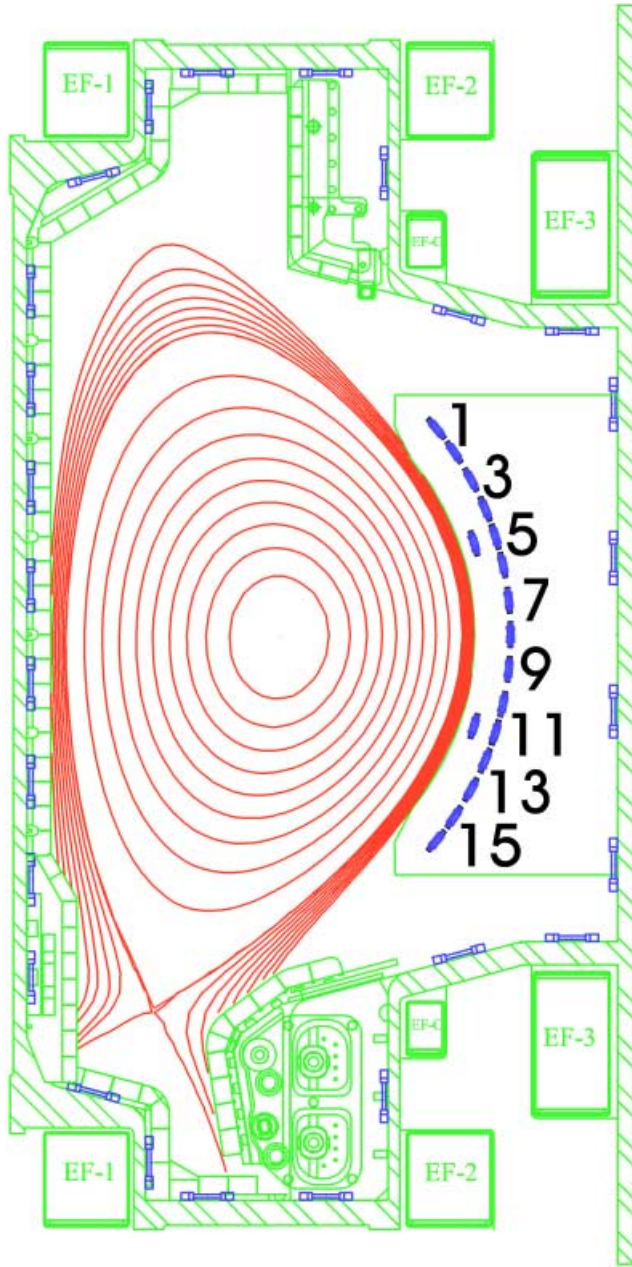


Fig. 15. Cross section of C-Mod showing the magnetic pickup coils (blue online) on one side of the full limiter and the main magnetic diagnostics (blue online) in the GH sector.

More recent data have been taken with 32 channels at a 2.5-MHz sampling rate for over 2 s with 14-bit resolution. This new data acquisition system can also take data at a sampling rate of up to 10 MHz.

The sensitivity of the combined coil and data acquisition system allows magnetic fluctuations to be measured down to  $\tilde{B}_\theta \sim 10^{-7}$  T up to the Nyquist frequency of half the sampling rate. The spacing of the coils allows toroidal mode numbers  $n$  up to 75 and poloidal mode numbers  $m$  up to 14 to be measured.

The measured frequency response of the coils has a 3-dB point around 1 MHz. This is limited by the 0.017-in.-thick stainless steel shield on the coils. This thickness is approximately one skin depth at 1 MHz.

In addition to the main magnetic fluctuation diagnostics, two probe heads were made that mount to the A-port scanning probe (see Sec. III.F.3) drive that contain magnetic pickup coils to measure short-wavelength ( $k_\theta \sim 1$  to  $5 \text{ cm}^{-1}$ ) modes in the plasma edge. The first head contained two poloidally separated Langmuir probes and one poloidally oriented magnetic pickup coil.<sup>65</sup> The coil was 5.8 mm in diameter and 4 mm long, had a surface area of  $17.6 \text{ cm}^2$ , and was made from a BN bobbin wound with 36 AWG (0.127-mm-diam), high-temperature ( $>450^\circ\text{C}$ ) Kulgrid ceramic-coated Ni-clad Cu wire (Ceramawire, Elizabeth City, North Carolina). The second probe head was instead made with two poloidally separated magnetic pickup coils a distance of 5.92 mm apart. The coils each had a surface area of  $11.3 \text{ cm}^2$  and were 3.3 mm long and 5.8 mm in diameter. The coil spacing allows estimates of  $m$  to be made up to 150.

## II.J. Phase-Contrast Imaging

The phase-contrast imaging (PCI) diagnostic measures electron density fluctuations line integrated along vertical chords. We use a 25-W cw  $\text{CO}_2$  laser, having a wavelength  $\lambda_0 = 10.6 \mu\text{m}$  and electric field amplitude  $E_0$ . The laser light is scattered off fluctuations having a wavenumber  $k_R$ , resulting in a separation of the scattered light from the unscattered beam. This separation is illustrated in Fig. 16, where the object plane is between the lenses. The electric field in this plane is given by

$$E_{image} = E_0 + E_0 \frac{i\Delta}{2} \exp(ik_R R) + E_0 \frac{i\Delta}{2} \exp(-ik_R R) , \quad (3)$$

where

$\Delta$  = acquired phase change,  $-\lambda_0 r_e l \tilde{n}_e$

$r_e$  = classical electron radius

$l$  = length of the chord

$\tilde{n}_e$  = density fluctuations.

By inserting a phase plate at the object plane, one shifts the phase of the unscattered beam by  $\pi/2$ , resulting in an additional multiplier on the first term in Eq. (3):

$$E_{image}^{PCI} = i \times E_0 + E_0 \frac{i\Delta}{2} \exp(ik_R R) + E_0 \frac{i\Delta}{2} \exp(-ik_R R) . \quad (4)$$

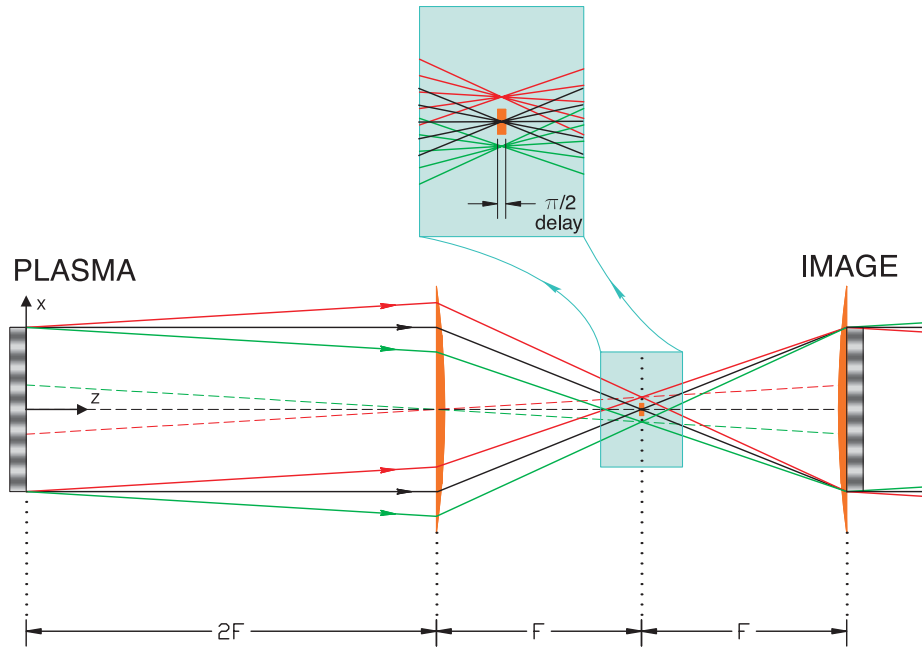


Fig. 16. Schematic drawing illustrating the PCI technique.

This phase contrast means that the observed intensity on the photoconductive HgCdTe detectors is

$$I_{\text{PCI}} = \frac{c}{8\pi} |E_{\text{image}}^{\text{PCI}}|^2 \approx \frac{c}{8\pi} |E_0|^2 [1 + 2\Delta \cos(k_R R)] \tag{5}$$

when  $|\Delta| \ll 1$ . The PCI method transforms phase to intensity variations.<sup>66</sup>

The number of PCI channels has recently been upgraded from 12 to 32. At the same time the 12-bit, 1-MHz data acquisition system was replaced by a 16-bit, 10-MHz cPCI setup. Further, new preamps were built having 3-dB points at 5 kHz and 15 MHz; these preamps also have a capability to increase the detector bias current up to the 35-mA detector specification (currently operating at 10 mA). Hardware such as the laser, phase plate, and preamps are PLC controlled.

The chord spacing and size is roughly 4 mm, so our coverage of  $R$  is 13 cm. The observable wave numbers can be resolved from 0.5 to 8  $\text{cm}^{-1}$ , and we can distinguish between waves traveling parallel and antiparallel to  $R$ . A setup using AOMs allows the observation of density fluctuations due to mode-converted ICRF waves in the 50- to 80-MHz range; broadband turbulence is observed simultaneously.

The PCI diagnostic can be used to study a large variety of physical processes: For example, the nature of broadband turbulence,<sup>67-72</sup> Alfvén cascades associated with low magnetic shear,<sup>73,74</sup> and mode-converted ICRF waves.<sup>75-79</sup> As an example of broadband turbulence mea-

surements we show a spectrogram of one of the PCI channels (passing through the core) in Fig. 17. High-frequency fluctuations above 2 MHz are observed at the

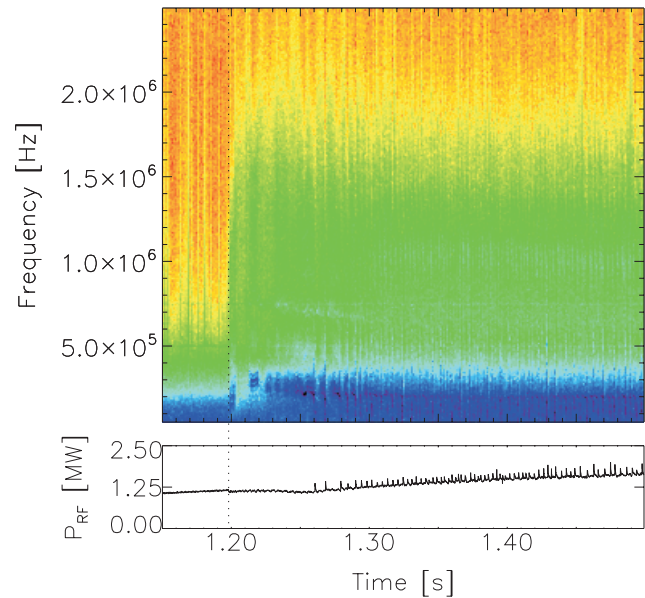


Fig. 17. Top: Spectrogram of a core PCI channel. The color scale is logarithmic (dark blue is high amplitude, red is low amplitude), the time resolution is 1 ms, and the frequency resolution is 5 kHz. The vertical dashed line marks the transition from L-mode to ELMY H-mode. Bottom: Trace of ICRF power.

transition from L-mode to edge-localized mode (ELMy) H-mode. Single ELMs are visible as vertical bursts, particularly in the 1.5-MHz range.

The CO<sub>2</sub> laser has just been replaced, bringing our laser power up to 60 W. Optics is being purchased to allow measurements at large wave numbers (up to 30 cm<sup>-1</sup>), and a technique to enable vertical localization of the signal will be implemented.<sup>80,81</sup>

## II.K. Reflectometry

Reflectometry has been widely used to measure density profiles and fluctuations in fusion machines.<sup>82</sup> In reflectometry, millimeter waves are launched toward the plasma and reflected at the cutoff layers. By comparing the signal amplitude and phase of the reflected waves with those of the launched waves, density profiles, fluctuation levels, and turbulence correlation lengths can be determined. In C-Mod, we have two reflectometry systems: The lower-frequency system has a frequency range from 50 to 110 GHz, and the higher-frequency system has frequencies of 132 and 140 GHz. Both systems are operated in the ordinary (O) mode, where the electric field of the wave is parallel to the magnetic field.

### II.K.1. Low-Frequency System

The lower-frequency system consists of five channels at frequencies of 50, 60, 75, 88, and 110 GHz. The cutoff densities are in the range of 0.31 to 1.5 × 10<sup>20</sup> m<sup>-3</sup>, which can be calculated from the simple equation

$$n_c(f_0) = (f_0/89.8)^2, \quad (6)$$

where  $f_0$  is in GHz and  $n_c$  is in units of 10<sup>20</sup> m<sup>-3</sup>. This system is configured as an amplitude-modulated (AM) reflectometer<sup>83,84</sup> (see Fig. 18). The group delay of the

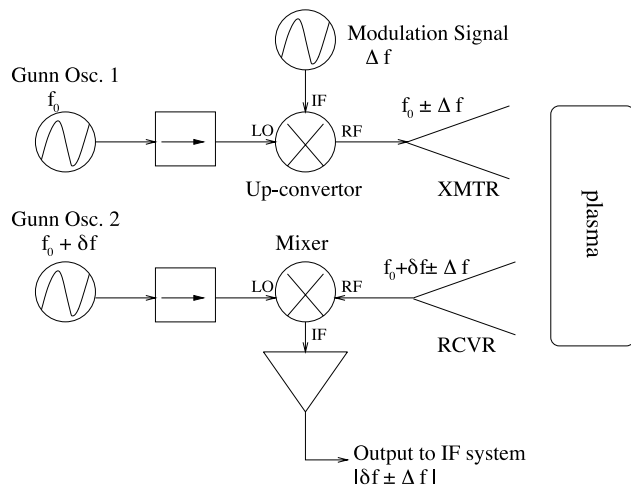


Fig. 18. Layout of the low-frequency millimeter wave system of the reflectometer.

wave is calculated from the phase difference between the AM-generated upper sideband ( $f_0 + \Delta f$ ) and lower sideband ( $f_0 - \Delta f$ ),  $d\phi/df \approx \Delta\phi/2\Delta f$ , where  $\Delta f$  is the modulation frequency. We can calculate the cutoff layer using the following equation:

$$R_c(f_0) = R_{edge} - \int_0^{f_0} \frac{c}{2\pi} \frac{d\phi}{df} \frac{df}{\sqrt{f_0^2 - f^2}}. \quad (7)$$

By combining Eqs. (6) and (7), a density profile can be obtained. The fluctuations of the group delay can also be used to monitor density fluctuations near the cutoff layer. The 88-GHz channel is specially configured so that it can measure both group delay and baseband fluctuations. The baseband fluctuations are used to monitor fluctuations more sensitively than the group delay fluctuations.<sup>85,86</sup>

The reflectometer provided edge profile measurements in both L- and H-mode plasmas. After the installation of the edge TS system, which has a better spatial resolution, the reflectometer is mainly used as a fluctuation diagnostic.

The reflectometer in C-Mod was the first diagnostic that observed the signature fluctuations, which was later dubbed the quasi-coherent mode, in the pedestal of EDA H-modes. The reflectometry observation clearly demonstrated that the quasi-coherent mode is associated with the EDA H-mode.<sup>84,86</sup> To help better interpret the reflectometry observations, a numerical 2-D code solving the Maxwell equations with the finite difference time domain scheme and a perfectly matched boundary layer was developed.<sup>87</sup> The code uses a unidirectional transparent method so that the reflected wave is separated from the total wave field. The simulation was able to invert the reflectometry observations to density fluctuation levels under some circumstances. The simulations also revealed that the reflectometry's sensitivity to the quasi-coherent mode, which has a rather small wavelength ( $k_\theta \sim 2$  to 6 cm<sup>-1</sup>) compared to the reflectometry beam size (a few centimeters), was due to an enhancement factor by the plasma curvature.<sup>88</sup>

### II.K.2. High-Frequency System

The two high-frequency reflectometer channels, operating at 132- and 140-GHz, respectively, are mainly used to probe density fluctuations in the core of the plasma when an ITB is present and at the edge when the H-mode barrier is sufficiently high.<sup>89</sup> The 132-GHz microwaves are reflected at a critical density of 21.6 × 10<sup>19</sup> m<sup>-3</sup> and the 140-GHz microwaves are reflected at 24.3 × 10<sup>19</sup> m<sup>-3</sup>. A heterodyne technique is used in these channels and each channel consists of two Gunn diodes, one generating the waves transmitted to the plasma and the other, which has a slightly different frequency (300 and 800 MHz for the 132- and 140-GHz channels, respectively), used as a local oscillator (see Fig. 19). Some power from the

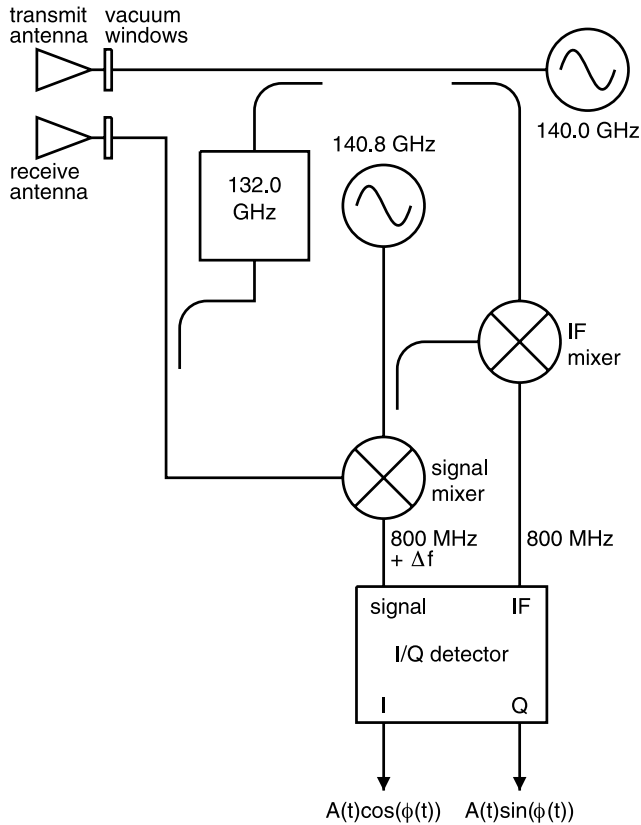


Fig. 19. Layout of the high-frequency millimeter wave system of the reflectometer.

main Gunn is used to generate the if reference frequency. The 132- and 140-GHz waves are combined with a 3-dB coupler into one waveguide that is then tapered to an oversized waveguide that transports the waves via a quartz window to the transmitting antenna inside the tokamak. A separate receiving antenna, which is mounted just below the transmission antenna, is connected to a second oversized waveguide to transport the reflected waves back to the microwave receiver. We have chosen separate transmission and receiving waveguides and antennas to avoid interference between spurious reflections of the incoming and the reflected waves. At the microwave receiver the waveguide is tapered down again to the fundamental mode, split in two, and fed to the 132- and 140-GHz receiver mixers. The if signal and reference frequency are connected to an in-phase quadrature (IQ) detector that yields the amplitude and phase of the reflected waves.

As an illustration of the high-frequency system, we show a spectrogram of the 132-GHz reflectometer in Fig. 20. The discharge and time window are the same as shown for PCI in Fig. 17. The highest density of the plasma is below cutoff up to 1.27 s, where reflection off the plasma commences. This is about 70 ms after the transition from L-mode to ELMy H-mode. For roughly 100 ms after cutoff is reached, ELMs are clearly ob-

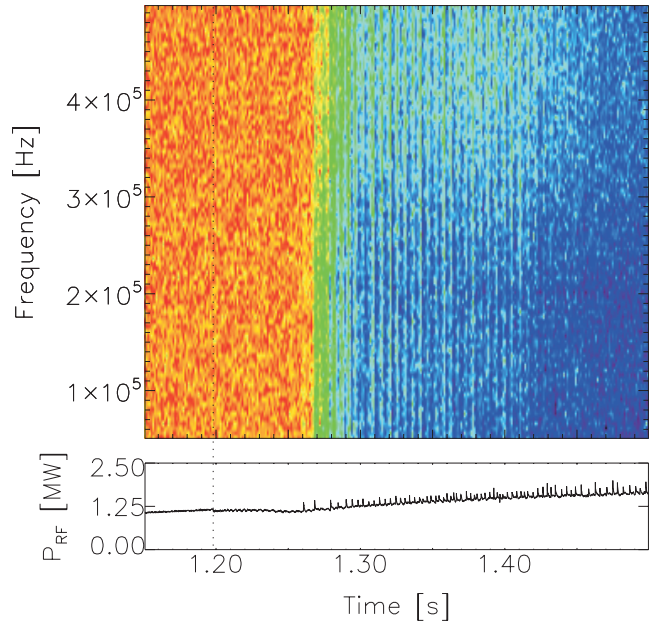


Fig. 20. Top: Spectrogram of the 132-GHz reflectometer channel. The color scale is logarithmic (dark blue is high amplitude, red is low amplitude), the time resolution is 1 ms, and the frequency resolution is 5 kHz. The vertical dashed line marks the transition from L-mode to ELMy H-mode. Bottom: Trace of ICRF power.

served as vertical bursts. The observed ELMs transition to featureless broadband turbulence between 1.4 and 1.45 s. Electron density profile measurements made using TS do not show a clear change in density, so the cause of this modification is not obvious. ELMs continue to exist until 1.5 s, as seen by, for example, PCI and  $D_\alpha$  light diodes. The TS data localize the reflectometer cutoff layer to be at midradius, well inside the pedestal region.

### III. PLASMA BOUNDARY

#### III.A. Video Cameras

C-Mod uses video cameras routinely for both scientific and operational purposes.<sup>90,91</sup> There are typically about six video cameras with views of the plasma. These cameras are generally quite small so that they can fit into reentrant tubes with views behind vacuum windows. They operate inside the toroidal field coils and as such are subjected to high  $B_\phi$ . Most of the cameras' images are distributed on a closed-circuit TV system, as well as being digitized and archived. The scientific uses for the cameras have included tomographic reconstructions of 2-D poloidal emissivities,<sup>92</sup> gas puff plume experiments,<sup>93,94</sup> diagnosis of the inboard scrape-off layer<sup>95</sup> (SOL) and divertor private flux zone,<sup>96</sup> and multifaceted asymmetric

radiation from the edge (MARFE) examinations,<sup>97</sup> providing constraints on divertor and edge simulations<sup>98,99</sup> and evaluations of the ion sink due to volume recombination in the divertor plasma. In addition to these scientific studies, the cameras serve as an aid for machine operation. With wide-view coverage of the plasma-facing components and in-vessel structures (e.g., the ICRF antennas and in-vessel hardware), the cameras are used as general plasma monitors, to identify impurity injection locations and to identify failures of in-vessel components. The view of one of the monitor cameras is shown in Fig. 21, in which plasma light illuminates the central column, two of the ICRF antennas, and a local in-vessel mirror used by another camera.

### III.B. Vacuum UV Spectrometry

C-Mod relies on quantitative analysis of emission spectra in the soft X-ray and vacuum ultraviolet spectral regions for diagnostic information, since much of the power radiated from the plasmas is emitted here. A time-resolving grazing-incidence spectrograph is used to monitor emission in these regions. It utilizes a microchannel plate and 1024-element diode array as its spectrally resolving detector. It has been used with 300, 600, and 1200 lines/mm gratings, providing spectral coverage from 8 to 170, 4 to 114, and 2 to 57 nm, respectively. With the 600 lines/mm grating, the best spectral resolution is 0.1 nm. The detector is moved from shot to shot to view from 4 to 9 nm of the spectral range at one time. The time resolution of the detector is programmable with a minimum of 2 ms. Since the informational content of the measured spectra is greater if the spectrograph sensitivity is absolutely calibrated, the instrument was calibrated between 2 and 12 nm using a low-power X-ray source with a proportional counter serving as an absolute detec-

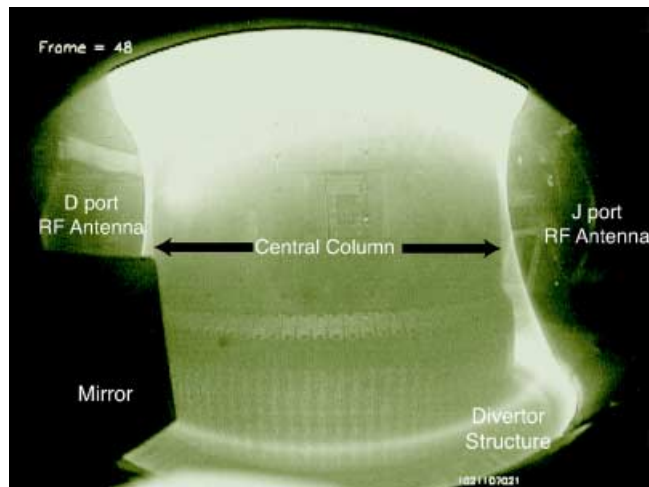


Fig. 21. Radially inward view from one of the survey cameras. The in-vessel hardware is as labeled.

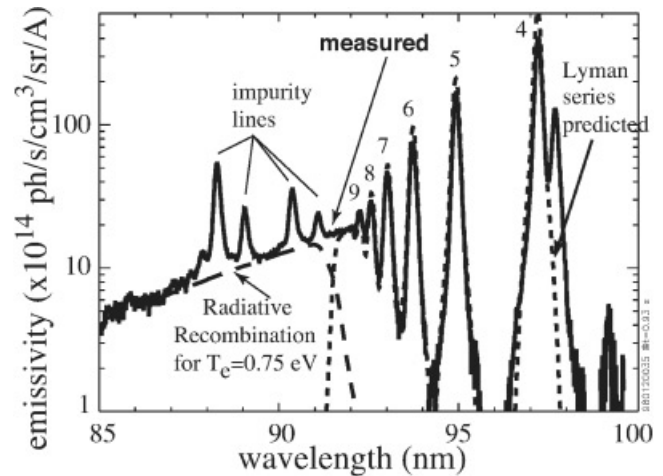


Fig. 22. Measured VUV spectrum of the high- $n$  H I Lyman series from the C-Mod divertor. Also shown are the spectra predicted for the Lyman series and the radiative recombination continuum.

tor.<sup>100</sup> In addition, in situ calibration using branching ratios is accomplished at several wavelengths from 25 to 102.6 nm using emission lines from H and He (Ref. 101).

The spectrograph has been utilized in a number of ways on C-Mod. It is a monitor of intrinsic impurities, typically B, C, O, F1, and Mo, as well as for impurities introduced into the plasma for diagnostic purposes (e.g., Ne, Ar, or metals injected via laser blowoff). The spectrograph has been used for studies of impurity transport, impurity penetration, and screening,<sup>102,103</sup> divertor power dissipation,<sup>5,104</sup> and divertor volume recombination and opacity and radiation transport of H Lyman series lines.<sup>105</sup> An example of a spectrum of the high- $n$  Lyman series is shown in Fig. 22, where the typical spectral resolution is shown and where a low electron temperature of 0.75 eV is obtained from the slope of the radiative recombination continuum emission coming from a detached divertor plasma.<sup>106</sup> Because of the strong interest in Mo (the plasma-facing components in C-Mod are Mo tiles), another instrument employing high-throughput multilayer mirrors has been used for dedicated monitoring of Mo emission at three different wavelengths.<sup>107</sup>

### III.C. Gas Puff Imaging

As part of our studies of the plasma edge and SOL, a set of optical diagnostics has been developed. In order to overcome the disadvantage of passive optical diagnostics, that of integrating emission along their lines of sight, we developed an experimental technique designated gas puff imaging<sup>108,109</sup> (GPI). Localized imaging is accomplished by viewing emission from a gas puff. Emission from the gas puff is typically much greater ( $\geq 5$  times) than any intrinsic emission along the line of sight. As

shown in the schematic of the GPI system, Fig. 23, the sight lines are configured to cross the gas puff, thus providing the spatial localization. Gas puff barrels are located on both the inboard and outboard side, near the plasma midplane and typically only 1 to 3 cm from the separatrix. The outboard gas puff is viewed by two arrays, one made using discrete fibers whose focal spots are arranged radially in front of the barrel and typically 3 to 4 mm in diameter. The fibers transmit light to filtered photodiodes with high sensitivity and flat frequency response for frequencies  $\leq 250$  kHz. A coherent fiber bundle is also employed to image the emission in front of the barrel in two dimensions. The view is parallel to the local magnetic field and thus images the structure of the emission perpendicular to the field. The 2-D image is transmitted either to movie cameras capable of very fast (up to 1-MHz) frame rates<sup>110</sup> or to gated snapshot cameras with high spatial resolution<sup>111</sup> (1 to 2 mm). Both of these GPI systems have been used to study edge and SOL turbulence as it is manifested in the emission.<sup>111,112</sup> An inboard gas puff is also viewed using a radially resolving array of fibers. The array views span the inboard separatrix and are used to compare the turbulence at the inboard side to that on the outboard side.<sup>112</sup>

### III.D. Visible Spectrometers

Owing to the suitability of their use with optical fibers both inside and outside the vacuum vessel, visible spectroscopic diagnostics are used extensively on C-Mod. By coupling multiple fibers to spectrometers with 2-D detectors, visible spectra from multiple views are routinely measured. An extensive system of views, including views of the divertor plates, inner wall, ICRF antennas, and limiters exists. The spectra measured using these views and spectrometers of medium ( $\Delta\lambda \sim 0.15$  nm) and

high ( $\Delta\lambda \sim 0.006$  nm) resolution have been used in a number of diagnostic applications. Typically, the views and spectrometers are absolutely calibrated so that absolute brightnesses are available. Some of the applications include the following:

- Determination of impurity source rates at various in-vessel locations<sup>113,114</sup>; these are valuable in studies of plasma-wall interactions, which include studies of impurity generation and screening.
- Diagnosis of three-body and radiative recombination in the divertor<sup>105,115–118</sup> and in MARFEs (Ref. 97).
- Measurements of  $n_e$  in regions where high- $n$  H Balmer series emission is strong.<sup>115,119–121</sup>
- Measurements of  $T_e$  (using the observed Saha-Boltzmann population of upper state levels) in regions where H Balmer series emission is strong.<sup>97</sup> An example of a high- $n$  Balmer series spectrum (from D in the divertor) is shown in Fig. 24, where density-broadened lines, recombination continuum, and an intensity distribution indicative of a Saha-Boltzmann population of the levels and of a recombining plasma are evident. Note that the Lyman series analog to this spectrum is shown in Fig. 22.
- Localization of  $D_\alpha$  emission using the Zeeman patterns.<sup>122</sup>
- Measurement of bulk flows of neutral H and ions, in both the SOL and divertor.<sup>123–125</sup>

### III.E. Soft X-Rays

The soft X-ray imaging system on C-Mod has four arrays, all at the same toroidal location. Each of these

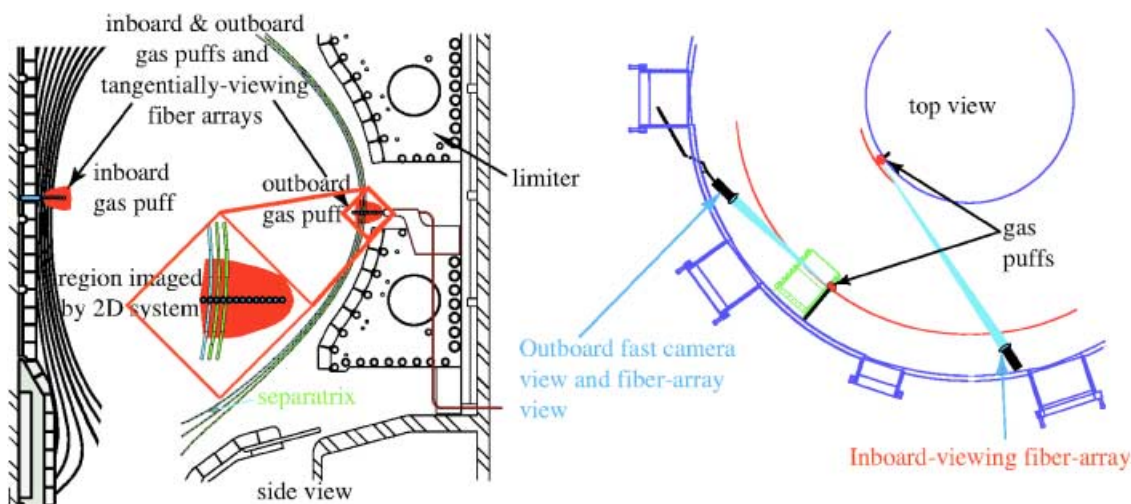


Fig. 23. Schematic of the GPI systems (side and top views).

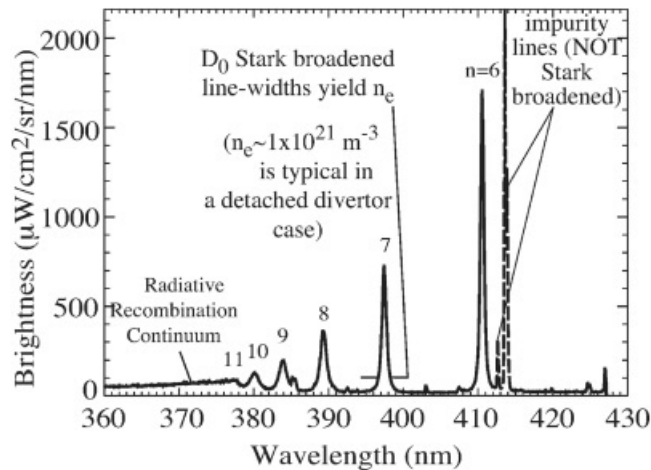


Fig. 24. Measured visible spectrum of the high- $n$  D Balmer series from a detached divertor plasma. Evident are the Stark-broadened Balmer lines, their intensity decrease according to a Saha-Boltzmann population of the upper levels and the radiative recombination continuum ( $\lambda < 370$  nm).

consists of a 38-element photodiode detector array from EG&G that fits in a standard 40-pin dual in-line package socket. The detectors were all relatively calibrated to 0.5% using the 5.9-keV Cu  $K_{\alpha}$  line from a commercial X-ray tube. To have sufficient coverage of the plasma cross section, the X-ray arrays were designed to be small enough to mount inside the vacuum vessel and therefore were constructed of materials suitable for ultrahigh vacuum and compatible with the 150°C bakeout.<sup>126</sup> The detectors are run with zero bias voltage (photovoltaic mode) to reduce the dark current while still affording a 3- $\mu$ s time response. X-ray photons hitting the detector elements yield a signal current (hundreds of nanoamperes to hundreds of microamperes) directly proportional to the absorbed photon energy flux. A Be foil over the collimating aperture of each array box filters out visible, UV, and ultrasoft X rays. The array components have been designed with very tight tolerance, press-fit pins between critical components so that the aperture, cover plate, and detector chip can all be removed and reassembled without changing the viewing geometry alignment. Since the arrays are contained in ultrahigh vacuum, the Be foils do not function as vacuum windows. This allows for optimization of the foil shape. The Be foil in each array is formed into a semicircular shape centered on the aperture so that each viewing chord passes through the same foil thickness. Originally, all four arrays were set up to each view the entire plasma cross section and the Be foils were chosen to be 50  $\mu$ m thick (2-keV 50% cutoff). More recently, one or two arrays have been modified to give a high-resolution view of the plasma edge for H-mode pedestal studies,<sup>127</sup> and these utilize 10- $\mu$ m Be foils (500-eV 50% cutoff), since the edge plasma is cooler

than the core. The signal current from each element is carried by a semirigid coaxial cable, with the coaxial shield at circuit ground. The 38 coaxial cables from each array are bundled together, surrounded with an electrically insulating sleeve, and inserted into a protective, flexible stainless steel conduit that is at machine ground. The conduits bring the coaxial bundles down through a vertical port to the underside of the machine, where each coaxial cable is attached to a coaxial vacuum feedthrough. The feedthrough flanges are electrically isolated from the machine. External coaxial cables feed the signals to transimpedance amplifiers, programmable gain amplifiers, and digitizers.

The multiple poloidal views of the core-viewing arrays allow for tomographic reconstruction of the local 2-D X-ray emissivity using a Fourier-Bessel expansion algorithm.<sup>128</sup> The radial spatial resolution is 2.5 cm. Tomographic reconstructions are done automatically between shots and archived along with the rest of the C-Mod data. More detailed reconstructions can also be done manually and saved as well.

To study the H-mode edge pedestal, one of the core X-ray arrays was modified to look at the plasma edge region with high spatial resolution by narrowing the view fan and using a much thinner Be window (10  $\mu$ m). This was accomplished by retrofitting a snoutlike structure onto the array box to move the collimating aperture much farther from the detector chip and decreasing the slit width in the poloidal direction.

### III.F. Probe Measurements

Figure 25 shows the locations of a number of probe diagnostics on C-Mod. These include fixed Langmuir probes (divertor probes and limiter flux probes), fast-scanning Langmuir probes (outer, vertical, and inner probes), a scanning gas puffing probe (vertical probe), a scanning magnetic probe (outer probe), divertor heat flux probes, and a movable ion mass spectrometer probe (omegatron).

#### III.F.1. Divertor Langmuir Probes

Langmuir probes are embedded into the surface of the inner and outer divertor plates. These consist of 4-mm-diam ceramic-coated Mo or W pins. Prior to the installation of new vertical plate geometry (August 2001), six triplets of three toroidally spaced probes were located at six poloidal locations in the inner divertor. Single probes at 16 poloidal locations are presently used (see Fig. 25). The outer divertor has triplets at 16 poloidal locations. The original intent of the triplet configuration was to infer plasma conditions using a triple-probe bias method<sup>129</sup> with each probe surface flush to the divertor surface [i.e., a flush-mount probe (FMP) array]. However, owing to problems associated with the interpretation of probe characteristics at small oblique field line angles,<sup>130</sup> one probe

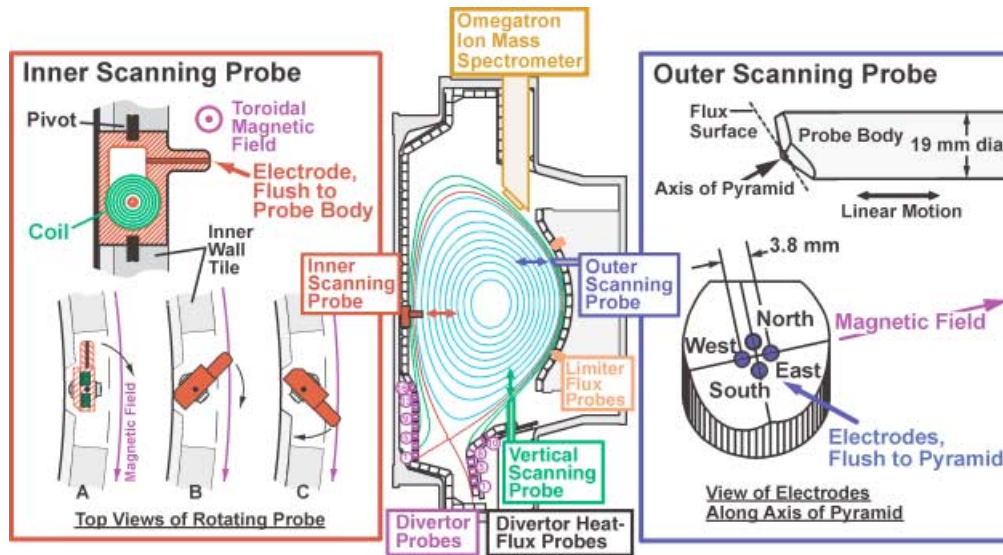


Fig. 25. Probe diagnostics on C-Mod.

in each triplet was converted to a proud geometry and operated in a conventional swept voltage manner. Before July 1995, Mo probes were used, extending 0.5 mm beyond the surface of the divertor and presenting a domed surface to the plasma flux. W replacements were installed by October 1995, also extending 0.5 mm beyond the surface but having a ramped surface, presenting a 10-deg angle with respect to incident field lines. Plasma density and temperature profiles across the divertor surface are typically deduced at 10-ms intervals by fitting current-voltage characteristics using standard magnetized probe theory.<sup>131</sup> The probes have operated continuously since the first C-Mod plasma in 1993, with periodic replacement of damaged (melted) electrodes. The probe arrays have provided vital information on divertor phenomena, including the physics of different parallel heat transport regimes and plasma detachment,<sup>132</sup> in/out divertor asymmetries and their connection to plasma drifts,<sup>133,134</sup> and thermoelectric currents.<sup>134</sup>

### III.F.2. Limiter Particle Flux Probes

To more fully investigate the phenomenon of main chamber recycling in C-Mod,<sup>135</sup> a set of eight probes was installed (May 2001) on each side of the two toroidally discrete outboard limiters in the device (one such limiter is shown in Fig. 25). They consist of 2-mm-diam W wires spanning a 14-mm zone from the leading edge into the limiter shadow. These particle flux probes are biased at a fixed negative voltage and measure the integral of the ion saturation flux density over the local SOL in contact with the limiter. Measurements from the probes have detected a high level of plasma flux to limiter surfaces, correlated

with the change in cross-field plasma transport as the collisionality of the edge plasma increases.<sup>136,137</sup>

### III.F.3. Outer Scanning Probe

Three different fast-scanning probes are presently used to record SOL plasma profiles up to the LCFS. A view of a standard probe head used on the outer scanning probe drive [also known as the A-port horizontal scanning probe (ASP) drive] is shown in Fig. 25. Facets are cut into the plasma-facing end of a 19-mm-diam Mo probe body to form a pyramidal surface. Four 1.5-mm-diam W electrodes penetrate the pyramid through holes at locations equidistant from the peak of the pyramid and coincident with the four edges of the pyramid. The W wires are insulated with ceramic coatings (0.18 mm thick) and cut so that their ends are flush to the pyramidal surface. This geometry is found to work well in the high power-density plasmas of C-Mod, since it presents a large surface area to heat flux flowing along magnetic field lines. The edges of the pyramid are oriented such that a magnetic field line that enters through the center of the west electrode proceeds through the pyramid and exits through the center of the east electrode. Thus, the east and west electrodes sample plasma from opposite directions along the same field line. In contrast, the north and south electrodes sample plasma from both directions on their respective magnetic field lines. The grazing angle between magnetic field lines and the pyramidal surfaces is approximately 20 deg and the pyramid is oriented so that all four electrodes lie on the same flux surface. The north and south electrodes are typically operated in a floating-voltage mode and the east and west electrodes in

a swept-voltage mode (2-kHz sweep,  $-300$ - to  $100$ -V maximum bias range with a 2-A clamp). By fitting positive and negative-going I-V characteristics, densities and temperatures along the trajectory of each probe are obtained every 0.25 ms (corresponding to  $\sim 0.25$  mm of probe travel). The east and west electrodes can also function as a Mach probe pair in which the plasma flow along the local magnetic field (the Mach number) can be estimated from the ratio of ion saturation currents.<sup>138</sup> In principle, this probe geometry can be used to infer fluctuation-induced particle fluxes by correlating fluctuations in poloidal electric field (north-south electrodes) with plasma density (east-west electrodes). However, a critical assessment of this measurement technique has revealed inconsistencies in the magnitude of the inferred particle flux,<sup>139</sup> suggesting that particle flux onto the probe head itself interferes with the measurement. Statistical analysis of plasma fluctuation data from this probe has yielded information on long-time correlations<sup>140</sup> and the universality of edge plasma fluctuations.<sup>141,142</sup> The outer scanning probe drive employs a removable probe head with a vacuum interlock, allowing the head assembly to be changed or repaired without breaking vacuum in the torus. This feature allows different probes to be used over the course of a run campaign. Specially designed magnetic probe heads with poloidal magnetic field pickup coils have been used (see Sec. II.I). By operating these probes close to the separatrix, high- $k_\theta$  magnetic fluctuations have been studied. Owing to their rapid decay with distance from the separatrix, these signals are otherwise difficult to detect. For example, data from a single-coil magnetic probe have revealed the electromagnetic character of the quasi-coherent mode seen near the separatrix in EDA H-mode discharges.<sup>65</sup> The latest magnetic probe design employs two coils to directly measure  $k_\theta$ . The probe drive has also been used to expose material samples to the plasma. The effectiveness of electron cyclotron discharge cleaning plasmas for removal of C deposits on first-wall materials has been studied this way.<sup>143</sup>

#### III.F.4. Vertical Scanning Probe

The vertical probe drive [also known as the F-port scanning probe (FSP) drive] does not have a vacuum interlock and therefore uses only one probe type. Its geometry and materials are similar to those of the outer probe head shown in Fig. 25 except that the spacing between W wires (Mo wires prior to July 1995) is a factor of 2 larger and the probe body is 16 mm in diameter. Starting September 1996, the probe head was modified to inject gaseous impurities through an orifice located at the center of the pyramid.<sup>144</sup> This system, in combination with CCD cameras looking at the dispersal patterns of resultant impurity plumes, has been used to explore plasma flows and impurity transport in the SOL (Ref. 145). These experiments also revealed information on perturbations in the plasma caused by the presence of the probe

(e.g., plasma recycling effects and probe-induced  $\mathbf{E} \times \mathbf{B}$  convection). Density, temperature, floating potential, and parallel flow information from the vertical scanning probe have been used to estimate cross-field profiles of both parallel and  $\mathbf{E} \times \mathbf{B}$  flows. By integrating the poloidal projection of these flows along the trajectory of the vertical scanning probe, the total particle flux directed toward the lower divertor structure has been studied. These measurements, combined with outer scanning probe data and midplane Lyman brightness measurements, have been used to estimate cross-field particle flux profiles in C-Mod and to infer scalings of particle transport coefficients. Details of the analysis technique can be found in Ref. 135.

#### III.F.5. Inner Scanning Probe

The newest addition to the scanning probe arsenal (June 2002) is the inner wall fast-scanning probe<sup>146</sup> (ISP) consisting of a single 1.6-mm-diam electrode, flush with the tip of a C fiber composite (CFC) arm (7.6-mm diameter) that protrudes from a rectangular CFC body (see Fig. 25). The probe body pivots about a vertical axis in response to current in an embedded coil that interacts with the ambient magnetic field, completing a 180-deg spin about its pivot axis. For angles less than 90 deg, the flush-mounted electrode samples plasma in one direction along a field line, while for angles greater than 90 deg, it samples the other. The single electrode is biased with respect to the graphite body, with a swept-voltage waveform. In a manner similar to that for the other scanning probes, cross-field profiles of density, temperature, and parallel Mach number are assembled. However, in this case the Mach number is computed from the ratio of the ion saturation current densities when the probe is looking upstream, rather than downstream, along magnetic field lines. Recent experiments utilizing the simultaneous operation of all three scanning probes have revealed remarkably fast (near-sonic) plasma flows along field lines in the high-field-side SOL and have connected the flow drive to ballooning-like cross-field transport physics.<sup>147</sup> These flows in the SOL are found to impose toroidal rotation boundary conditions on the confined plasma that depend on X-point topology, suggesting an explanation for the X-point dependence of the L-H power threshold.<sup>148</sup>

#### III.F.6. Divertor Heat Flux Probes

Standard infrared thermography of the divertor structures is difficult in C-Mod, due to the lack of line-of-sight views of surfaces in the closed divertor geometry. A novel method for measuring heat fluxes to the surface of the divertor<sup>149</sup> based on an adaptation of a commercially available thermocouple device (Nanmac Corp., Framingham, Massachusetts) was therefore investigated. The adapted design employs a coaxial-like geometry with a ceramic-coated W-Re ribbon embedded in a 6.35-mm-diam Mo rod. The end of the rod is aligned with the outer

divertor tiles, exposing a 5-deg ramped surface to incident magnetic field lines. A thermocouple junction (W-Re/Mo) is formed at the plasma-facing end of the rod as the ceramic insulation breaks down there (first by machining the end of the rod, then by plasma interaction). Using a 1-D, semi-infinite slab model, heat fluxes parallel to field lines in the range of 50 to 500 MW m<sup>-2</sup> can be inferred from the surface temperature evolution. An array of 10 units [called the fast-thermocouple (TC) array] was deployed (June 1996) on the outer divertor, at locations similar to those of the outer divertor probes (shown in Fig. 25). Representative traces of surface temperature and parallel heat flux profiles at five positions for a discharge with 3 MW of ICRF heating are shown in Fig. 26. The peak parallel heat flux during the L-mode phase (before 0.67 s) was measured to be in the range of 400 MW m<sup>-2</sup>. Electrical noise from the plasma environment limits the sensitivity and time response of these sensors to 10 ms. Nevertheless, these experiments have demonstrated the utility of the device for the measurement of high heat fluxes. The sensors are readily adaptable for W first-wall materials and may be employed in future divertor upgrades to C-Mod.

### III.F.7. Omegatron Ion Mass Spectrometer

In situ ion mass spectrometry is a valuable tool for monitoring intrinsic or extrinsic impurities in the tokamak plasma and to assess first-wall conditions by means of associated plasma chemistry. However, the high  $B_\phi$  in C-Mod ( $\leq 8$  T), which are prototypical of a power-producing fusion reactor, prohibit the use of ion mass spectrometry based on ion orbit discrimination (see Ref. 150). For this reason, an ion mass spectrometer was developed<sup>151</sup> based on the principle of resonant ion collection in an omegatron device.<sup>152</sup> Figure 27 shows the arrangement of key components in the C-Mod omegatron probe. An entrance slit extracts a ribbon beam of ions from the plasma, which first encounters a series of grids (controlling parallel energy) and then passes into an rf cavity. Ions, whose cyclotron frequency is resonant with the applied rf waves, increase their Larmor radii and are collected on the rf plates. By sweeping over a range of frequencies, an  $M/Z$  ion spectrum is produced. Information about the impurity ion temperatures is also obtained. A spectrum from a prototype version of the omegatron is shown in Fig. 27. This is the first time that such a device has been operated in a high-magnetic field fusion experiment, demonstrating its utility in monitoring impurities with  $M/Z$  up to 12 ( $B_\phi \sim 4$  T). In a novel set of experiments, this spectrometer was used to infer cross-field transport rates for He ions in the SOL by measuring local concentrations of singly and doubly ionized <sup>3</sup>He (Ref. 153). Improvements to the grid arrangement and shielding have been identified and implemented. Experimentation with the improved device has not yet been performed.

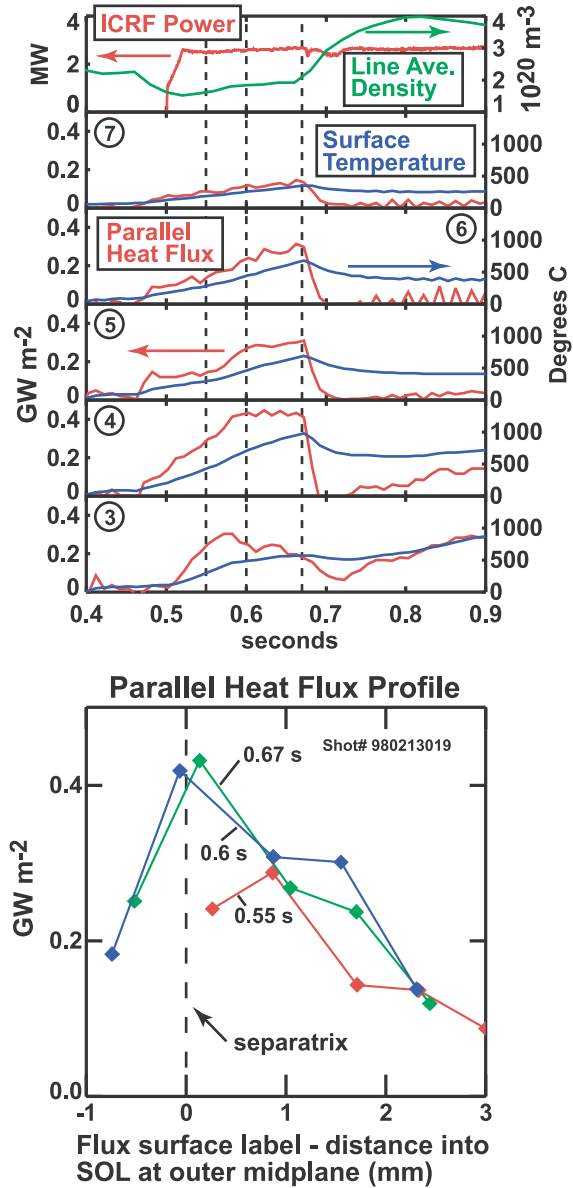


Fig. 26. Data traces from divertor heat flux probes (top) and resultant parallel heat flux profiles at three times in the discharge (bottom). Circled numbers indicate probe locations on the divertor (see Fig. 25).

## IV. WAVES

### IV.A. H/D Isotope Measurements

The density ratio of H to D ions in the confined plasma is important for several reasons. Primary among them is that the efficiency of single-pass absorption of ICRF fast waves, in the minority damping regime, depends sensitively on the fractional abundance of the minority species.<sup>154,155</sup> In a majority of C-Mod discharges, H minority heating ( $f \sim 80$  MHz,  $B_\phi \sim 5$  T) is used.

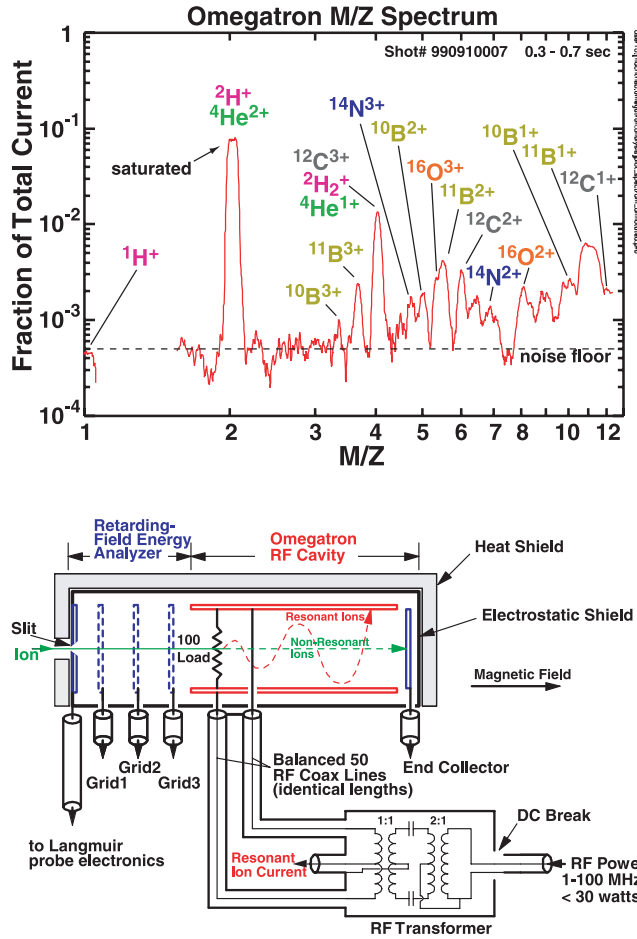


Fig. 27. Typical M/Z ion spectrum from the omegatron probe (top) and arrangement of grids and rf cavity (bottom).

Mode conversion processes also depend on the isotope mix.<sup>156</sup> Finally, the isotope mix can be used to study wall recycling and the efficacy of wall-conditioning techniques. The H to D ratio in C-Mod is routinely measured through high-resolution visible spectroscopy that monitors the relative intensities of H and D Balmer emission. This necessarily looks at the ratio in the recycling edge neutrals and does not directly probe the ion abundance. It does provide excellent trend data, and insofar as H and D have the same penetration probability and confinement in the core plasma, it also gives quantitative information for the ion ratio. The experimental technique is described in detail in Ref. 157 and is summarized here. Spectra are obtained using a 1-m double-slit Ebert spectrograph. The plasma is viewed horizontally, just below the midplane. The light is first filtered through a linear polarizer, oriented to pass horizontal (parallel to the toroidal field) polarization, which is dominated by the unshifted  $\pi$  lines in the Zeeman multiplets. A 0.1-mm-diam quartz fiber then transfers the light to the entrance slit of the spectrometer. The detector is a 128-element Reticon photo-

diode array, capable of readout in 10 ms and having a spectral coverage from 655 to 657 nm. Typical spectra are acquired with a 50-ms integration time. The system is calibrated with a D/H arc lamp. The resolution of the spectrometer system is 0.027 nm FWHM (the separation between the H and D lines is 0.176 nm). A typical spectrum from a plasma discharge is shown in Fig. 28. In this case, the H minority concentration, deduced from the relative brightness amplitudes of the two lines, is about 5%. To automate the analysis, a robust algorithm was developed that does not rely on nonlinear iterative fits to multiple spectral lines. Instead, the intensity-weighted mean of the spectrum is simply calculated, and its location in-between the two main peaks determines the relative intensities:

$$\frac{I_H}{I_D} = \frac{\bar{\lambda} - \lambda_D}{\lambda_H - \bar{\lambda}}, \quad (8)$$

where  $\bar{\lambda}$  is the weighted mean. For typical measured intensities, this approach is usually reliable for minority fractions greater than about 2%, with an uncertainty of about 1%.

#### IV.B. Compact Neutral Particle Analyzer

The recently installed compact neutral particle analyzer (CNPA) is designed to provide ICRF minority tail temperature measurements for low- to moderate-density ( $n_e < 2 \times 10^{20} \text{ m}^{-3}$ ) C-Mod D(H) plasmas.

The CNPA uses Si diodes to detect charge-exchanged (CX) energetic ( $>30\text{-keV}$ ) neutral particles for diagnosis of the ICRF H minority tail temperature. A 50-ms DNB, upgraded to 1.5 s in 2006, provides the majority of the neutrals for the CX process. However, for very low density ( $n_e \sim 6 \times 10^{19} \text{ m}^{-3}$ ) C-Mod plasmas, sufficient

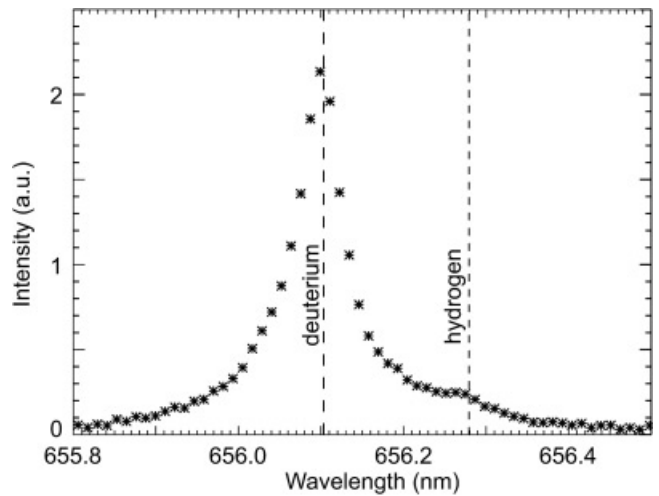


Fig. 28. Typical H/D Balmer- $\alpha$  spectrum, showing the locations of the D (majority) and H (minority) peaks.

signal is detected even without the use of a beam. Fast digitization techniques are used to perform postshot energy pulse-height analysis (PHA) to extract the minority H energy spectrum.

Currently, the diagnostic consists of a single Ortec R-015-050-100 detector mounted on a vertical port with an on-axis view of the plasma and a viewing cone diameter of 1.5 cm at the midplane. The detector is 3.6 m away from the midplane machine axis (see Fig. 29). A filter wheel allows the use of 1- and 10- $\mu\text{m}$  Be filters for X-ray detection or testing purposes, and a manual micrometer controls the aperture size. The electronics consists of an eV Products 5093 preamp followed by an Ortec 472 amplifier. The signal is digitized by a 14-bit cPCI board operated at 10 MHz over the entire shot. PHA of the signal is performed via Matlab programs postshot. This arrangement served as the primary CNPA setup during its shakeout period in the spring 2004 campaign.

Numerous noise issues initially plagued the operation of the CNPA. These fall into two categories: electrical pickup and plasma background. For the CNPA, the former mainly results from the equilibrium field coils, DNB, and a 500-kHz beat frequency of the D and E port ICRF antennas. The ability to review the amplifier voltage for the entire shot is very helpful in diagnosing these pickup problems. For the second category, the plasma background consists of visible light to X-rays, CX neutral particles from bulk ions, neutrons, and gamma rays. The Si detector has a varying degree of sensitivity to all of these background sources. This background noise in

terms of emissivity can be significant even for moderate-density C-Mod plasmas, since these densities are very high compared to other fusion plasmas that have successfully employed this type of diode NPA (Refs. 158 and 159). Moreover, the intrinsic signal-to-noise ratio in C-Mod is weakened by greater attenuation of both the neutral particle signal and the DNB in these denser plasmas, and because the C-Mod neutral beam is considerably weaker in power than the typical heating beam used for this kind of diagnostic elsewhere. Slight mitigation of this background problem stems from the use of either a thin attenuating foil or a dead layer on the detector (2000 Å Al equivalent) to block out the visible light, low-energy (<10 keV for D) bulk neutral particles and a small amount of the soft X rays. This layer, however, increases the energy threshold for resolvable neutrals and decreases the signal resolution because of straggling. Due to both the plasma background and electrical pickup issues, the current CNPA is so far operational only for low-density C-Mod plasmas ( $n_e < 1 \times 10^{20} \text{ m}^{-3}$ ). Figure 30 illustrates the raw neutral signals detected for such a plasma. After accounting for the CX cross section, beam and neutral attenuation, and dead layer straggling, these spectra determine the minority tail temperature and hence the ICRF power deposition.

The diagnostic will be upgraded by installing three additional detectors, providing multiple sightlines, one being a tangential view that results in significantly higher cross sections for high-energy (>100-keV) CX. Additionally, the preamp and amplifier electronics will be integrated and made significantly more compact, which should decrease electrical pickup. These improvements, along with the new long-pulse DNB, should allow the

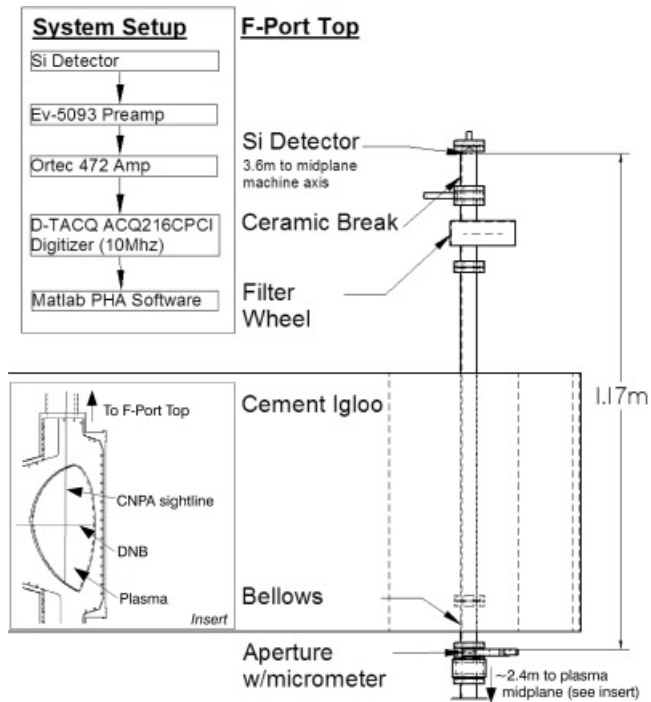


Fig. 29. CNPA schematic during the spring 2004 campaign.

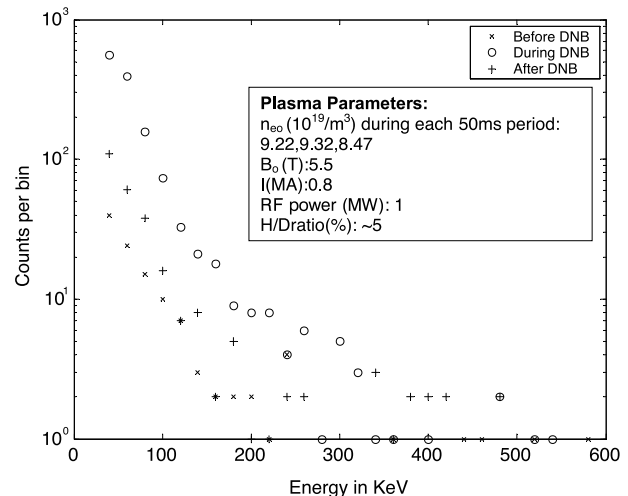


Fig. 30. CNPA signal during low-density L-mode C-Mod discharge 1040415006. The three sets of data shown are counts from 50 ms before, during, and after the DNB fires. Clearly, the DNB increases the CNPA signal significantly.

CNPA to give spatiotemporal tail temperature measurements for moderate-density ( $n_e \sim 2 \times 10^{20} \text{ m}^{-3}$ ) C-Mod D(H) plasmas.

#### IV.C. Hard X-Rays

An LHCD system has been installed on C-Mod, allowing the exploration of advanced tokamak regimes. The location of the LHCD is critical to advanced tokamak performance and may be dynamically adjusted through  $n_{||}$  spectral control. The current deposition profile may be inferred by measuring the nonthermal bremsstrahlung emission in the hard X-ray (HXR) region. The resulting current profile shape will be compared to results from ray-tracing codes such as accurate calculation of consistent MHD equations<sup>160</sup> (ACCOMME). Information about the electron distribution function may also be gathered through the use of a Fokker-Planck solver and a model involving LHCD quantities determined from the HXR measurements.<sup>161</sup>

Following the work of Ref. 162, a pinhole camera will be used to image energies in the 20- to 250-keV range. Thirty-two solid-state CdZnTe detectors provide good efficiency and resolution in a small package necessary to meet the space constraints of the access port. Detectors and pulse-processing electronics are integrated into a compact and modular package, making extensive use of printed circuit board and surface mount technology. A preamp and shaper are needed to convert the pulses into a digitizable form. A six-pole Gaussian filter and a line driver were developed to give output pulses of about  $1 \mu\text{s}$  in width and a sensitivity of 12 mV/keV.

An ambient environment of neutrons, gamma rays, and high ICRF power requires careful shielding. All elec-

tronics are mounted together in a box that is mounted inside a 1.5-in.-thick Pb gamma ray shield. Monte Carlo simulations of neutron and photon transport were done to study the shield thickness using the Monte Carlo  $N$ -particle transport code.<sup>163</sup> The shield is composed of an inner and an outer Al skin that is filled by a lead pour to eliminate any joints and bolt holes. The whole assembly is mounted on a rail system for positioning and to allow other diagnostic access (see Fig. 31).

The system will make use of fast digitization and software signal processing techniques.<sup>164</sup> Fast digitization offers great flexibility for data processing and reduction. Pulses are digitized at a rate of 10 MHz for the entire shot and then stored locally. A PHA routine is then used to generate spectra for user-specified time and energy bins. The PHA routine can also be used to reduce pileup through fitting and to improve noise reduction. After PHA the chordal measurements for a given energy may be inverted to give the radial emissivity profile. A dedicated server will be used to process the large data sets. Fokker-Planck modeling uses the local emissivity from the HXR measurement and the bremsstrahlung cross sections to generate a distribution function that is characterized by parameters such as the quasi-linear diffusion coefficient and plateau width. This information will be used to adjust the lower-hybrid power level and  $n_{||}$  spectrum to attain desirable advanced tokamak plasmas.

### V. MACROSTABILITY

#### V.A. Equilibrium Magnetics

The equilibrium magnetic diagnostics on C-Mod consist of the standard set found on many tokamaks. Because

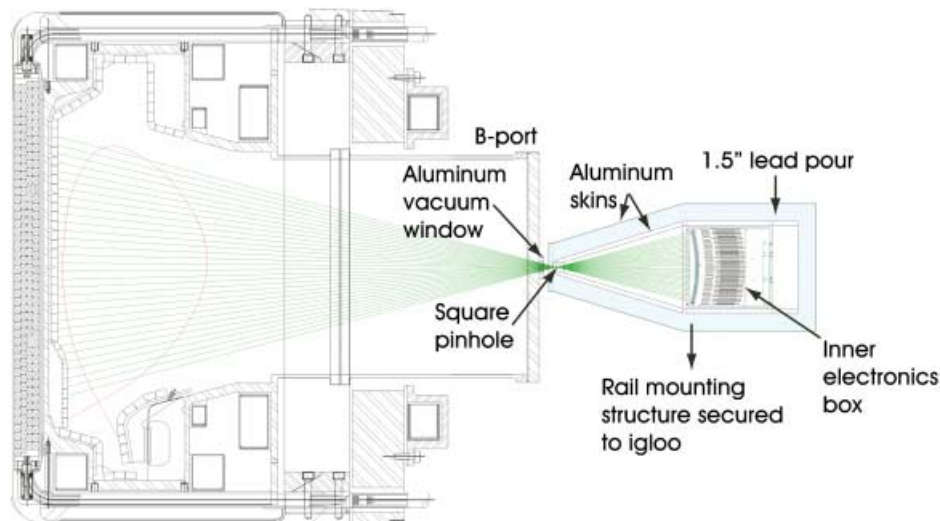


Fig. 31. Setup of the hard X-ray camera.

the thick-walled vacuum vessel is effectively a highly conducting shell, all of the sensors are located in-vessel in order for them to have an acceptable time response. Teflon-insulated wire is used because it is compatible with both ultrahigh vacuum and with the prescribed bake-out temperatures of 150°C. Nearly all of the in-vessel sensors are mounted on the vessel wall surface. In areas of the vessel wall that are protected with Mo tiles, channels have been machined into the back of the tiles to accommodate the magnetic sensors, leads, and thermal shields. The leads from each sensor consist of twisted pairs (several twists per centimeter) and run continuously to the vacuum interface feedthroughs with no splices inside the machine.

There are four principal types of equilibrium magnetic sensors in C-Mod:

1.  $B_\theta$  coils
2. flux loops (including saddle loops and diamagnetic loops)
3.  $B_\phi$  coils (including diamagnetic compensation coils)
4. Rogowski coils.

The  $B_\theta$  coils measure the local poloidal magnetic field parallel to the vacuum vessel wall. Each  $B_\theta$  coil consists of several hundred turns on a ceramic bobbin, with dimensions of 30 mm in length and 8 mm in diameter and an effective sensing area of 67 cm<sup>2</sup>. There are sets of  $B_\theta$  coils at four different toroidal locations, with each set comprised of 26 coils distributed fairly uniformly around the poloidal perimeter of the vessel (see Fig. 15). The coils are attached to the wall by resistance (spot) welding. The spatial location of the  $B_\theta$  coils is known with an accuracy of 0.5 mm on the inboard portion of the vessel and  $\sim 2$  mm on the outboard surface. All  $B_\theta$  coils and their leads are covered by a thin stainless steel shield (attached by resistance welds) for protection from the plasma (even under the tiles). The sensitivity of each coil was calibrated to 0.5% on the bench before being installed in the machine.

The flux loops each consist of a single loop of wire inside small-diameter (0.8- and 1.6-mm) stainless steel tubes that are resistance welded to the vessel wall. The full poloidal flux loops each consist of one toroidal turn, distributed at 21 different locations around the poloidal perimeter of the vessel. For those poloidal locations where a full flux loop is not feasible, such as across port regions, rectangular partial flux loops (also known as saddle coils) measure radial flux on the outboard wall (four loops) and one flux loop each on both the ceiling and the floor of the machine. The partial plus full flux loops effectively give the poloidal flux at 26 ( $R, z$ ) locations around the poloidal perimeter. The choice of 26  $B_\theta$  and 26 flux measurements was based on a theoretical and computational study<sup>165</sup> that showed that this number of sensors is more than sufficient to accurately reconstruct

the magnetic equilibrium and still allow for redundancy in case some sensors fail. An additional two pairs of saddle coils are placed at the outboard vessel midplane, with each element in the pair located on opposite toroidal sides of the vessel, in order to detect  $n = 1$  and 2 radial flux patterns (locked modes). Finally, two flux loops are wrapped around the poloidal perimeter of the machine at two different toroidal locations in order to measure the total toroidal flux (plasma plus vacuum), which is part of the diamagnetic measurement.

The  $B_\phi$  coils are used to measure the vacuum toroidal field. These consist of two pairs of robust stainless steel mandrels that are bolted onto tabs that are tungsten inert gas welded to the vessel wall. The pairs are at two different toroidal locations, and the elements of each pair are symmetrically located on the top and bottom of the machine and are oriented to measure the toroidal magnetic flux. The bottom mandrels are behind the outer divertor modules and the top mandrels are behind the gusset plates. The mandrels are slotted so as to prevent induced currents in their structure. Each mandrel has two coils wound on it that measure the vacuum toroidal field. The large number of redundant coils allows for some of them to be hardwired into a cancellation circuit to null out the vacuum field measured by the diamagnetic coil signal. The  $B_\phi$  coil sensitivities were calibrated to 0.5% on the bench.

There are two Rogowski coils in the vacuum vessel for measuring the plasma current. Their design and fabrication was more complicated than those of the other magnetics components because they had to closely fit the shape of the poloidal perimeter (1-mm tolerance), which essentially dictated having a flexible Rogowski coil. Due to the requirements for ultrahigh vacuum and vessel bake-out, one of the few acceptable flexible materials for use as a coil-winding mandrel is Teflon, which unfortunately has an unacceptably large thermal expansion coefficient. A novel design and fabrication technique was developed to overcome this problem. Thick-walled Teflon tubes (outer diameter of 6.35 mm, inner diameter of 1.6 mm) were cut to lengths equal to half the poloidal perimeter (about 180 cm). A lightly threaded Cu rod (1.6-mm diameter) was screwed into the central hole through the entire length of the Teflon tube. This Cu core prevented the thermal expansion of the Teflon coil mandrel and also served as the central return wire for the Rogowski coil. The threading operation required heating the Teflon tube to 180°C to expand the central hole enough for the Cu rod to be threaded through the full 180-cm length. The Rogowski coils were calibrated in the lab and found to have a mutual inductance of  $2.53 \times 10^{-8}$  H to currents flowing within their closed loop and less than 0.1% of that sensitivity to currents flowing outside of them and to  $B_\phi$ .

All of the magnetics signals are proportional to the time derivatives of magnetic fields or currents. For equilibrium reconstruction, which require magnetic fields,

magnetic fluxes, and plasma current, all of the signals have to be integrated. Since the signals are also used for real-time control of the plasma, the integration has to be done in real time. On C-Mod, this is accomplished with fairly standard, differential-input op-amp integrators that have a sample-and-hold circuit to set and reset the baseline. Baseline drift over the C-Mod pulse length is negligible. Integrator circuit time constants (inverse of gain) range from 6.7 ms for the  $B_\theta$  coils up to 1 s for the full flux loops and several seconds for the  $B_\phi$  coils. A subset of approximately 60 coils also goes through isolation amplifiers to the hybrid computer that performs the real-time control of the plasma.

For the standard between-shot EFIT equilibrium reconstruction, the magnetic diagnostics described are used along with the active coil currents measured by Rogowski coils on the buswork between the power supplies and each coil. For more specialized applications, EFIT is also run with input from kinetic diagnostics, including TS ( $n_e$  and  $T_e$ ), ECE ( $T_e$ ), and TCI ( $n_e$ ). In a few cases, soft X-ray emission (pedestal location) and MSE measurements (internal poloidal magnetic field) have also been employed.

The equilibrium magnetics system has been in operation now for more than a dozen years, with an excellent performance record. The few signal failures that have occurred are primarily due to intermittent conductivity faults at the vacuum feedthrough connectors during disruptions.

### V.B. Active MHD Antennas

A pair of active MHD antennas was installed at one toroidal location to actively excite low-amplitude (total  $\tilde{B}_r \sim 1 \times 10^{-4}$  T) MHD modes in the frequency range  $1 \text{ kHz} < f_{\text{active}} < 1 \text{ MHz}$  (Ref. 166). Figure 32a shows a

poloidal cross section of C-Mod with the location of the two antennas relative to the outboard limiter and a typical plasma equilibrium. Figure 32b shows a photo of the antennas and limiter as installed. Each antenna consists of five turns that are  $15 \times 25$  cm in area. The windings are 0.25-in.-wide and 0.125-in.-thick plates that are laser cut from stainless steel and then welded together at each turn. The windings are protected from the plasma by insulating BN tiles, which allow the last turn closest to the plasma to be only 2.5 cm from the limiter radius. The windings are secured to the antenna frame with ceramic-coated stainless steel bolts, and the turns are insulated from one another and the frame with ceramic-coated stainless steel washers and mica washers for added high-voltage standoff. These are particularly important to avoid rf breakdown across the antenna because of the strong coupling ( $-23$  dB) to the 4-MW ICRF antenna located  $\sim 40$  cm away (just visible in the lower right-hand side of the photo) in the frequency range 50 to 80 MHz. The active MHD antennas are connected to 15-kV/15-A coaxial feedthroughs via ceramic-beaded coaxial transmission lines. The constant current rating of the feedthroughs is 15 A. Note that the feedthroughs can easily exceed their constant current rating for the pulse lengths we have on C-Mod. It is a thermal rating, and it takes some time for them to overheat. A geometrical calculation of the toroidal mode spectrum of each antenna indicates that they excite a broad range of toroidal mode numbers, as shown in Fig. 32c, with a FWHM of  $|n| \sim 16$ . In the frequency range of interest ( $< 1$  MHz), each antenna remains inductive, with a resistance of up to  $1 \Omega$  and an inductance of  $9 \mu\text{H}$ . One side of each antenna is grounded to the vacuum vessel at the coaxial vacuum feedthrough to help reduce the ICRF transmission out the vacuum feedthrough. Just on the air side of the feedthrough, each antenna is connected to 10-kW low-pass rf filters that

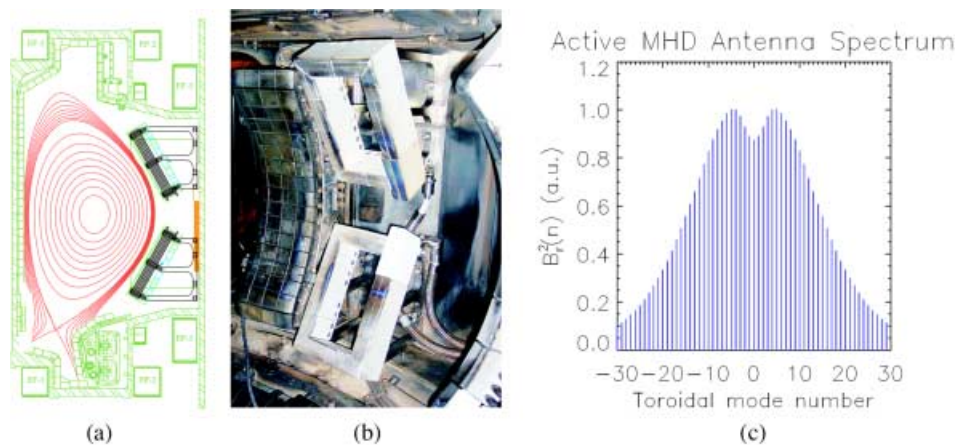


Fig. 32. (a) Poloidal cross section of C-Mod showing the locations of the two active MHD antennas relative to the outboard limiter and a typical plasma equilibrium, (b) photo of the active MHD antennas in C-Mod, and (c) calculated active MHD antenna toroidal mode spectrum with a FWHM of  $|n| \sim 16$ .

attenuate the ICRF frequencies by as much as  $-90$  dB while leaving frequencies below 1 MHz essentially unaffected in both amplitude and phase.

The antennas are driven by a pair of MIT-designed amplifiers that, when properly matched, can excite the antenna with up to 20 A across the frequency range from a few kHz to nearly 1 MHz. Initially, the matching network consisted of parallel and series capacitances tuned to a particular frequency with a FWHM of only  $\pm 50$  kHz around the peak frequency. The narrow bandwidth of the matching circuit meant that the plasma resonances were most easily observed when exciting the antenna at a constant frequency and that the frequency could not be swept over a broad range to search for a resonance. The system has been upgraded to automatically switch capacitors to change the frequency range and maintain substantial matching across a much broader frequency range. In addition, a stereo audio amplifier has been used to drive up to 65-A peak current in both antennas over the audio range of frequencies below 20 kHz, where matching networks are unnecessary.

As an example, the calculated radial field perturbation produced by one active MHD antenna driven with 10 A of current is  $\tilde{B}_r \sim 5 \times 10^{-5}$  T at a distance of 12 cm from the antenna or  $r/a \sim 0.5$ . So, the perturbations produced by the active MHD antenna can be observed only by rather sensitive magnetic diagnostics and do not otherwise perturb the plasma equilibrium.

## VI. OUTLOOK

Diagnostics on fusion devices are constantly evolving; sometimes existing systems are removed to make port space available for new diagnostics. One has to prioritize and focus on measuring quantities consistent with the needs of the overall program. Among the systems that have been removed are the neutral particle analyzer, the D pellet injector, the laser blowoff impurity injector, and a dedicated VUV multilayer mirror tuned to a Na-like Mo line.

A number of C-Mod diagnostics are currently in the planning or early operational stage:

1. A new high-resolution ( $\lambda/\Delta\lambda \sim 2000$ ) X-ray spectrometer has been installed.<sup>167</sup> The system was designed to measure impurity temperature and poloidal velocity based on emission line spectra from He-like Ne ( $1s^1 2p^1 \rightarrow 1s^2$ ) in a narrow spectral band centered on  $\lambda = 13.65$  Å. The instrument was mounted with a radial view below the midplane ( $r/a \sim 0.8$ ). This view allows for impurity temperature and poloidal rotation profile measurements in the pedestal region.

2. We are planning a polarimeter/interferometer system that will use the proposed International Thermonuclear Experimental Reactor (ITER) geometry with

poloidal views and retroreflectors on the inner wall. The final system will most likely operate in the far-infrared range, but a prototype system operating at  $10.6 \mu\text{m}$  is now in operation on C-Mod. This system has proved that excellent density measurements can be made, that the vibration levels are acceptable, and that shuttering and protection of the retroreflectors is essential for reliable operation. Pneumatic shutters are being developed for the inner-wall retroreflector array.

3. We are working on installing a quartz crystal microbalance (QCM). These are used in the coating industry and can measure thicknesses of deposition down to a fraction of an angstrom. Our aim is to use a movable QCM to map out the deposition pattern of the boronization. This would be invaluable in understanding how fast we are eroding the B during discharges and how we might most efficiently coat surfaces in preparation for our best discharges. We will locate the boronization resonance layer at different major radii and measure the deposition rate at the QCM location for different orientations of the sensor.

4. We are in the planning stages for implementing a differential frequency reflectometry diagnostic to measure density profiles and fluctuations local to an ICRF antenna. Our plan includes probes near the top and bottom of the ICRF antenna—a diagnostic similar to this has recently been added to the ITER diagnostics list. The frequency range will be 92 to 120 GHz initially with a planned upgrade to 140 GHz. The magnetic field and density are similar to the expected ITER values, thus making the reflectometer a valuable prototype.

To conclude the paper, we note that since C-Mod operates at magnetic field strengths and densities comparable to the ITER design parameters, our diagnostics work has perspectives and implications far beyond C-Mod.

## ACKNOWLEDGMENTS

The authors are very grateful to T. W. Fredian and J. A. Stillerman for data acquisition assistance and thank the Alcator C-Mod Operations and ICRF groups for expert running of the tokamak.

This work was supported at MIT by the U.S. Department of Energy, cooperative grant DE-FC02-99ER54512.

## REFERENCES

1. I. H. HUTCHINSON et al., *Phys. Plasmas*, **1**, 1511 (1994).
2. J. A. STILLERMAN, T. W. FREDIAN, K. A. KLARE, and G. MANDUCHI, *Rev. Sci. Instrum.*, **68**, 939 (1997).
3. K. F. MAST, J. C. VALLET, C. ANDELFINGER, P. BETZLER, H. KRAUS, and G. SCHRAMM, *Rev. Sci. Instrum.*, **62**, 744 (1991).
4. R. L. BOIVIN, J. A. GOETZ, E. S. MARMAR, J. E. RICE, and J. L. TERRY, *Rev. Sci. Instrum.*, **70**, 260 (1999).

5. J. A. GOETZ et al., *Phys. Plasmas*, **3**, 1908 (1996).
6. R. L. BOIVIN et al., *Phys. Plasmas*, **7**, 1919 (2000).
7. C. L. FIORE and R. L. BOIVIN, *Rev. Sci. Instrum.*, **66**, 945 (1995).
8. J. WESSON, *Tokamaks*, Oxford University Press, Oxford, United Kingdom (1997).
9. J. D. HUBA, *NRL Plasma Formulary*, Naval Research Laboratory (2004).
10. T. C. HSU, PhD Thesis, Massachusetts Institute of Technology (1993).
11. A. E. HUBBARD, T. C. HSU, and P. J. O'SHEA, *Proc. 9th Joint Workshop on Electron Cyclotron Emission and Electron Cyclotron Heating*, Borrego Springs, California, p. 387, World Scientific (1995).
12. T. C. HSU, A. E. HUBBARD, and I. H. HUTCHINSON, *Proc. 8th Joint Workshop on Electron Cyclotron Emission and Electron Cyclotron Heating*, Gut Ising, Germany, Vol. 2, p. 409, World Scientific (1992).
13. S. GUHARAY and D. BOYD, *Rev. Sci. Instrum.*, **61**, 3520 (1990).
14. P. J. O'SHEA and A. E. HUBBARD, *Proc. 9th Joint Workshop on Electron Cyclotron Emission and Electron Cyclotron Heating*, Borrego Springs, California, p. 393, World Scientific (1995).
15. P. J. L. O'SHEA, PhD Thesis, Massachusetts Institute of Technology (1997).
16. P. O'SHEA, P. BONOLI, A. HUBBARD, M. PORKOLAB, and Y. TAKASE, *Proc. 12th Topl. Conf. Radio Frequency Power in Plasmas*, Savannah, Georgia, Vol. 403, p. 89, American Institute of Physics (1997).
17. Y. IN, PhD Thesis, Massachusetts Institute of Technology (2000).
18. Y. IN et al., *Nucl. Fusion*, **40**, 1463 (2000).
19. Y. IN, A. E. HUBBARD, and I. H. HUTCHINSON, *Plasma Phys. Control. Fusion*, **43**, 645 (2001).
20. A. E. HUBBARD, R. L. BOIVIN, J. F. DRAKE, M. GREENWALD, Y. IN, J. H. IRBY, B. N. ROGERS, and J. A. SNIPES, *Plasma Phys. Control. Fusion*, **40**, 689 (1998).
21. A. E. HUBBARD et al., *Phys. Plasmas*, **5**, 1744 (1998).
22. G. TAYLOR, C. K. PHILLIPS, G. SCHILLING, J. R. WILSON, A. HUBBARD, S. J. WUKITCH, and E. NELSON-MELBY, *Bull. Am. Phys. Soc.*, **43**, 1821 (1998).
23. A. JANOS, M. MCCARTHY, E. FREDRICKSON, K. MCGUIRE, and G. TAYLOR, *Rev. Sci. Instrum.*, **66**, 668 (1995).
24. J. W. HEARD et al., *Rev. Sci. Instrum.*, **70**, 1011 (1999).
25. R. J. CHATTERJEE, P. E. PHILLIPS, J. HEARD, C. WATTS, R. GANDY, and A. HUBBARD, *Fusion Eng. Design*, **53**, 113 (2001).
26. A. G. LYNN, PhD Thesis, University of Texas at Austin (2004).
27. A. G. LYNN, P. E. PHILLIPS, and A. E. HUBBARD, *Rev. Sci. Instrum.*, **75**, 3859 (2004).
28. A. E. HUBBARD et al., *Plasma Phys. Control. Fusion*, **46**, A95 (2004).
29. C. WATTS and R. GANDY, *Phys. Rev. Lett.*, **75**, 451 (1995).
30. C. WATTS, Y. IN, J. HEARD, P. PHILLIPS, A. LYNN, A. HUBBARD, and R. GANDY, *Nucl. Fusion*, **44**, 987 (2004).
31. R. WATTERSON and K.-I. CHEN, *Rev. Sci. Instrum.*, **61**, 2867 (1990).
32. D. A. MOSSESIAN, A. HUBBARD, and J. IRBY, *Rev. Sci. Instrum.*, **70**, 759 (1999).
33. J. W. HUGHES, D. MOSSESIAN, K. ZHUROVICH, M. DeMARIA, K. JENSEN, and A. HUBBARD, *Rev. Sci. Instrum.*, **74**, 1667 (2003).
34. J. W. HUGHES, D. A. MOSSESIAN, A. E. HUBBARD, E. S. MARMAR, D. JOHNSON, and D. SIMON, *Rev. Sci. Instrum.*, **72**, 1107 (2001).
35. L. L. LAO, H. ST. JOHN, R. D. STAMBAUGH, A. G. KELLMAN, and W. PFEIFFER, *Nucl. Fusion*, **25**, 1611 (1985).
36. T. N. CARLSTROM, J. C. DeBOO, R. EVANKO, C. M. GREENFIELD, C.-L. HSIEH, R. T. SNIDER, and P. TROST, *Rev. Sci. Instrum.*, **61**, 2858 (1990).
37. D. DIMOCK, B. GREK, D. JOHNSON, B. LaBOMBARD, B. LIPSCHULTZ, and G. McCRACKEN, *Rev. Sci. Instrum.*, **68**, 700 (1997).
38. J. SHEFFIELD, *Plasma Scattering of Electromagnetic Radiation*, Academic, New York (1975).
39. A. C. SELDEN, *Phys. Lett. A*, **79**, 6 (1980).
40. J. HOWARD, B. M. JAMES, and W. I. B. SMITH, *J. Phys. D.*, **12**, 1435 (1979).
41. H. RÖHR, *Phys. Lett.*, **81A**, 451 (1981).
42. F. FLORA and L. GIUDICOTTI, *Appl. Opt.*, **26**, 4001 (1987).
43. J. H. IRBY, E. S. MARMAR, E. SEVILLANO, and S. M. WOLFE, *Rev. Sci. Instrum.*, **59**, 1568 (1988).
44. M. E. FOORD, E. S. MARMAR, and J. L. TERRY, *Rev. Sci. Instrum.*, **53**, 1407 (1982).
45. J. E. RICE and E. S. MARMAR, *Rev. Sci. Instrum.*, **61**, 2753 (1990).
46. J. E. RICE, F. BOMBARDA, M. A. GRAF, E. S. MARMAR, and Y. WANG, *Rev. Sci. Instrum.*, **66**, 752 (1995).
47. J. E. RICE, F. BOMBARDA, M. A. GRAF, E. S. MARMAR, J. L. TERRY, and Y. WANG, *Fusion Eng. Design*, **34-35**, 159 (1997).
48. J. E. RICE, J. L. TERRY, E. S. MARMAR, and F. BOMBARDA, *Nucl. Fusion*, **37**, 241 (1997).
49. J. E. RICE et al., *Nucl. Fusion*, **44**, 379 (2004).
50. J. E. RICE et al., *J. Phys. B*, **29**, 2191 (1996).
51. B. LIPSCHULTZ, D. A. PAPPAS, B. LaBOMBARD, J. E. RICE, D. SMITH, and S. J. WUKITCH, *Nucl. Fusion*, **41**, 585 (2001).
52. J. A. GOETZ, C. S. PITCHER, B. LaBOMBARD, B. LIPSCHULTZ, J. E. RICE, and J. L. TERRY, *Nucl. Fusion*, **41**, 1751 (2001).
53. S. A. KOREPANOV et al., *Rev. Sci. Instrum.*, **75**, 1829 (2004).
54. V. I. DAVYDENKO, *Nucl. Instrum. Methods Phys. Res. A*, **427**, 230 (1999).
55. W. L. ROWAN, M. B. SAMPSELL, and R. S. GRANETZ, *Rev. Sci. Instrum.*, **75**, 3487 (2004).
56. E. C. EISNER and W. L. ROWAN, *Rev. Sci. Instrum.*, **72**, 1004 (2001).
57. A. ÖLME, *Physica Scripta*, **1**, 256 (1970).
58. D. I. SIMON, N. L. BRETZ, E. MARMAR, R. BRAVENEC, and R. F. PARSELLS, *Proc. 18th Symp. Fusion Engineering*, Albuquerque, New Mexico, p. 349, IEEE/NPSS (1999).
59. N. BRETZ et al., *Rev. Sci. Instrum.*, **72**, 1012 (2001).
60. H. Y. YUH, PhD Thesis, Massachusetts Institute of Technology (2005).
61. F. M. LEVINTON, R. J. FONCK, G. M. GAMMEL, R. KAITA, H. W. KUGEL, E. T. POWELL, and D. W. ROBERTS, *Phys. Rev. Lett.*, **63**, 2060 (1989).

62. R. J. FONCK, P. A. DUPERREX, and S. F. PAUL, *Rev. Sci. Instrum.*, **61**, 3487 (1990).
63. G. R. McKEE et al., *Rev. Sci. Instrum.*, **70**, 913 (1999).
64. J. A. SNIPES et al., *Plasma Phys. Control. Fusion*, **44**, 381 (2002).
65. J. A. SNIPES et al., *Plasma Phys. Control. Fusion*, **43**, L23 (2001).
66. A. MAZURENKO, PhD Thesis, Massachusetts Institute of Technology (2001).
67. A. MAZURENKO, M. PORKOLAB, D. MOSESSIAN, J. A. SNIPES, X. Q. XU, and W. M. NEVINS, *Phys. Rev. Lett.*, **89**, 225004 (2002).
68. L. LIN et al., *Bull. Am. Phys. Soc.*, **48**, 97 (2003).
69. D. R. ERNST et al., *Proc. 20th IAEA Fusion Energy Conf.*, Vilamoura, Portugal, IAEA-CN-116/TH/4-1, International Atomic Energy Agency (2004).
70. L. LIN et al., *Bull. Am. Phys. Soc.*, **49**, 73 (2004).
71. N. P. BASSE et al., *Bull. Am. Phys. Soc.*, **49**, 217 (2004).
72. N. P. BASSE et al., *Phys. Plasmas*, **12**, 052512 (2005).
73. E. M. EDLUND et al., *Bull. Am. Phys. Soc.*, **49**, 73 (2004).
74. J. A. SNIPES et al., *Phys. Plasmas*, **12**, 056102 (2005).
75. E. A. NELSON-MELBY, PhD Thesis, Massachusetts Institute of Technology (2001).
76. E. NELSON-MELBY, M. PORKOLAB, P. T. BONOLI, Y. LIN, A. MAZURENKO, and S. J. WUKITCH, *Phys. Rev. Lett.*, **90**, 155004 (2003).
77. Y. LIN et al., *Phys. Plasmas*, **11**, 2466 (2004).
78. S. J. WUKITCH et al., *Phys. Plasmas*, **12**, 056104 (2005).
79. Y. LIN et al., *Plasma Phys. Control. Fusion*, **47**, 1207 (2005).
80. A. TRUC et al., *Rev. Sci. Instrum.*, **63**, 3716 (1992).
81. S. KADO et al., *Jpn. J. Appl. Phys.*, **34**, 6492 (1995).
82. R. NAZIKIAN, G. J. KRAMER, and E. VALEO, *Phys. Plasmas*, **8**, 1840 (2001).
83. P. C. STEK, PhD Thesis, Massachusetts Institute of Technology (1997).
84. Y. LIN, PhD Thesis, Massachusetts Institute of Technology (2001).
85. J. H. IRBY, S. HORNE, I. H. HUTCHINSON, and P. C. STEK, *Plasma Phys. Control. Fusion*, **35**, 601 (1993).
86. Y. LIN, J. IRBY, P. STEK, R. NAZIKIAN, I. HUTCHINSON, J. SNIPES, and M. MCCARTHY, *Rev. Sci. Instrum.*, **70**, 1078 (1999).
87. Y. LIN, J. IRBY, R. NAZIKIAN, E. MARMAR, and A. MAZURENKO, *Rev. Sci. Instrum.*, **72**, 344 (2001).
88. Y. LIN, R. NAZIKIAN, J. H. IRBY, and E. S. MARMAR, *Plasma Phys. Control. Fusion*, **43**, L1 (2001).
89. N. P. BASSE et al., *Bull. Am. Phys. Soc.*, **48**, 54 (2003).
90. C. J. BOSWELL, J. L. TERRY, B. LIPSCHULTZ, and J. STILLERMAN, *Rev. Sci. Instrum.*, **72**, 935 (2001).
91. C. J. BOSWELL, PhD Thesis, Massachusetts Institute of Technology (2003).
92. C. J. BOSWELL and J. L. TERRY, *IEEE Trans. Plasma Sci.*, **30**, 78 (2002).
93. D. JABLONSKI et al., *J. Nucl. Mater.*, **241–243**, 782 (1997).
94. S. GANGADHARA and B. LaBOMBARD, *J. Nucl. Mater.*, **313–316**, 1167 (2003).
95. C. J. BOSWELL, J. L. TERRY, B. LaBOMBARD, B. LIPSCHULTZ, and C. S. PITCHER, *Plasma Phys. Control. Fusion*, **46**, 1247 (2004).
96. C. J. BOSWELL, J. L. TERRY, B. LaBOMBARD, B. LIPSCHULTZ, and J. A. GOETZ, *J. Nucl. Mater.*, **290–293**, 556 (2001).
97. B. LIPSCHULTZ, J. L. TERRY, C. J. BOSWELL, A. HUBBARD, B. LaBOMBARD, and D. A. PAPPAS, *Phys. Rev. Lett.*, **81**, 1007 (1998).
98. S. LISGO, PhD Thesis, University of Toronto (2003).
99. S. LISGO et al., *J. Nucl. Mater.*, **337–339**, 139 (2005).
100. J. L. TERRY, H. L. MANNING, and E. S. MARMAR, *Proc. SPIE Conf.*, San Diego, California, Vol. 689, p. 54, International Society for Optical Engineering (1986).
101. H. OHKAWA, RR-97-11, Massachusetts Institute of Technology, Plasma Science and Fusion Center (1997).
102. G. M. McCRACKEN et al., *Phys. Plasmas*, **4**, 1681 (1997).
103. R. S. GRANETZ et al., *J. Nucl. Mater.*, **241–243**, 788 (1997).
104. J. A. GOETZ et al., *Phys. Plasmas*, **6**, 1899 (1999).
105. J. L. TERRY et al., *Phys. Plasmas*, **5**, 1759 (1998).
106. J. L. TERRY, B. LIPSCHULTZ, C. J. BOSWELL, D. A. PAPPAS, A. YU. PIGAROV, S. I. KRASHENINNIKOV, and B. LaBOMBARD, *Proc. 26th Conf. Controlled Fusion and Plasma Physics*, Maastricht, The Netherlands, Vol. 23J, p. 325, European Physical Society (1999).
107. M. J. MAY et al., *Nucl. Fusion*, **37**, 881 (1997).
108. J. L. TERRY et al., *J. Nucl. Mater.*, **290**, 757 (2001).
109. R. J. MAQUEDA et al., *Rev. Sci. Instrum.*, **72**, 931 (2001).
110. J. L. TERRY et al., *Rev. Sci. Instrum.*, **75**, 4196 (2004).
111. S. J. ZWEBEN et al., *Phys. Plasmas*, **9**, 1981 (2002).
112. J. L. TERRY et al., *Phys. Plasmas*, **10**, 1739 (2003).
113. D. A. PAPPAS, B. LIPSCHULTZ, B. LaBOMBARD, M. J. MAY, and C. S. PITCHER, *J. Nucl. Mater.*, **266–269**, 635 (1999).
114. B. LIPSCHULTZ, D. A. PAPPAS, B. LaBOMBARD, J. E. RICE, D. SMITH, and S. WUKITCH, *J. Nucl. Mater.*, **290–293**, 286 (2001).
115. D. LUMMA, J. L. TERRY, and B. LIPSCHULTZ, *Phys. Plasmas*, **4**, 2555 (1997).
116. B. LIPSCHULTZ et al., *Phys. Plasmas*, **6**, 1907 (1999).
117. J. L. TERRY et al., *J. Nucl. Mater.*, **266–269**, 30 (1999).
118. B. LIPSCHULTZ, J. L. TERRY, C. BOSWELL, S. I. KRASHENINNIKOV, B. LaBOMBARD, and D. A. PAPPAS, *J. Nucl. Mater.*, **266–269**, 370 (1999).
119. B. WELCH et al., *Phys. Plasmas*, **2**, 4246 (1995).
120. A. YU. PIGAROV, J. L. TERRY, and B. LIPSCHULTZ, *Plasma Phys. Control. Fusion*, **40**, 2051 (1998).
121. A. YU. PIGAROV, J. L. TERRY, and B. LIPSCHULTZ, *Proc. 24th Conf. Controlled Fusion and Plasma Physics*, Berchtesgaden, Germany, Vol. 21A, p. 573, European Physical Society (1997).
122. J. L. WEAVER et al., *Rev. Sci. Instrum.*, **71**, 1664 (2000).
123. B. L. WELCH, J. L. WEAVER, H. R. GRIEM, W. A. NOONAN, J. TERRY, B. LIPSCHULTZ, and C. S. PITCHER, *Phys. Plasmas*, **8**, 1253 (2001).
124. J. GHOSH et al., *Phys. Plasmas*, **11**, 1033 (2004).
125. K. MARR, B. LIPSCHULTZ, B. LaBOMBARD, and J. L. TERRY, *J. Nucl. Mater.*, **337–339**, 286 (2005).

126. T. SUNN PEDERSEN and R. S. GRANETZ, *Rev. Sci. Instrum.*, **70**, 586 (1999).
127. T. SUNN PEDERSEN, R. S. GRANETZ, A. E. HUBBARD, I. H. HUTCHINSON, E. S. MARMAR, J. E. RICE, and J. TERRY, *Nucl. Fusion*, **40**, 1795 (2000).
128. L. WANG and R. S. GRANETZ, *J. Opt. Soc. Am. A*, **10**, 2292 (1993).
129. S. L. CHEN and T. SEKIGUCHI, *J. Appl. Phys.*, **36**, 2363 (1965).
130. G. F. MATTHEWS, S. J. FIELDING, G. M. McCracken, C. S. PITCHER, P. C. STANGEBY, and M. ULRICKSON, *Plasma Phys. Control. Fusion*, **32**, 1301 (1990).
131. P. C. STANGEBY, in *Plasma Diagnostics*, Vol. 1, p. 157, Academic Press, Boston (1989).
132. B. LaBOMBARD et al., *Phys. Plasmas*, **2**, 2242 (1995).
133. I. H. HUTCHINSON et al., *Plasma Phys. Control. Fusion*, **38**, A301 (1996).
134. B. LaBOMBARD et al., *J. Nucl. Mater.*, **241–243**, 149 (1997).
135. B. LaBOMBARD et al., *Nucl. Fusion*, **40**, 2041 (2000).
136. B. LaBOMBARD et al., *Phys. Plasmas*, **8**, 2107 (2001).
137. B. LaBOMBARD et al., *Proc. 19th IAEA Fusion Energy Conf.*, Lyon, France, IAEA-CN-94/EX/D2-1, International Atomic Energy Agency (2003).
138. I. H. HUTCHINSON, *Phys. Rev. A*, **37**, 4358 (1988).
139. B. LaBOMBARD, *Phys. Plasmas*, **9**, 1300 (2002).
140. B. A. CARRERAS, V. E. LYNCH, and B. LaBOMBARD, *Phys. Plasmas*, **8**, 3702 (2001).
141. G. Y. ANTAR, G. COUNSELL, Y. YANG, B. LaBOMBARD, and P. DEVYNCK, *Phys. Plasmas*, **10**, 419 (2003).
142. B. PH. VAN MILLIGEN et al., *Phys. Plasmas*, **12**, 052507 (2005).
143. R. T. NACHTRIEB, B. L. LaBOMBARD, J. L. TERRY, J. C. REARDON, W. L. ROWAN, and W. R. WAMPLER, *J. Nucl. Mater.*, **266–269**, 896 (1999).
144. B. LaBOMBARD et al., *J. Nucl. Mater.*, **266–269**, 571 (1999).
145. S. GANGADHARA and B. LaBOMBARD, *Plasma Phys. Control. Fusion*, **46**, 1617 (2004).
146. N. SMICK, B. LaBOMBARD, and C. S. PITCHER, *J. Nucl. Mater.*, **337–339**, 281 (2005).
147. B. LaBOMBARD et al., *Nucl. Fusion*, **44**, 1047 (2004).
148. B. LaBOMBARD et al., *Phys. Plasmas*, **12**, 056111 (2005).
149. S. GANGADHARA, B. LaBOMBARD, B. LIPSCHULTZ, and N. PIERCE, *Bull. Am. Phys. Soc.*, **41**, 1550 (1996).
150. G. F. MATTHEWS, *Plasma Phys. Control. Fusion*, **31**, 841 (1989).
151. R. NACHTRIEB, B. LaBOMBARD, and E. THOMAS, Jr., *Rev. Sci. Instrum.*, **71**, 4107 (2000).
152. J. HIPPLE, H. SOMMER, and H. THOMAS, *Phys. Rev.*, **72**, 1877 (1949).
153. R. NACHTRIEB and B. LaBOMBARD, *Phys. Plasmas*, **7**, 4573 (2000).
154. J. ADAM, *Plasma Phys. Control. Fusion*, **29**, 443 (1987).
155. Y. TAKASE, P. T. BONOLI, S. N. GOLOVATO, and M. PORKOLAB, *Proc. 11th Topl. Conf. Radio Frequency Power in Plasmas*, Palm Springs, California, Vol. 289, p. 56, American Institute of Physics (1995).
156. Y. LIN et al., *Plasma Phys. Control. Fusion*, **45**, 1013 (2003).
157. T. E. TUTT, MS Thesis, Massachusetts Institute of Technology (1999).
158. M. OSAKABE et al., *Rev. Sci. Instrum.*, **72**, 788 (2001).
159. A. G. ALEKSEYEV et al., *Rev. Sci. Instrum.*, **74**, 1905 (2003).
160. P. BONOLI, M. PORKOLAB, J. J. RAMOS, W. NEVINS, and C. KESSEL, *Plasma Phys. Control. Fusion*, **39**, 223 (1997).
161. J. DECKER and Y. PEYSSON, *Proc. 29th Conf. Controlled Fusion and Plasma Physics*, Montreux, Switzerland, Vol. 26B, p. P-4.052, European Physical Society (2002).
162. Y. PEYSSON and F. IMBEAUX, *Rev. Sci. Instrum.*, **70**, 3987 (1999).
163. J. BRIESMEISTER, LA-13709-M, Los Alamos National Laboratory (2000).
164. R. O'CONNELL, D. J. DEN HARTOG, C. B. FOREST, and R. W. HARVEY, *Rev. Sci. Instrum.*, **74**, 2001 (2003).
165. S. P. HAKKARAINEN and J. P. FREIDBERG, RR-87-22, Massachusetts Institute of Technology, Plasma Science and Fusion Center (1987).
166. J. A. SNIPES, D. SCHMITTDIEL, A. FASOLI, R. S. GRANETZ, and R. R. PARKER, *Plasma Phys. Control. Fusion*, **46**, 611 (2004).
167. A. INCE-CUSHMAN, J. E. RICE, M. BITTER, S. G. LEE, and M. L. REINKE, *Bull. Am. Phys. Soc.* (2005).